2011

Controlled growth of organic semiconductor films in liquid

Daniel W. (Daniel Wainwright) Shaw
Western Washington University

Controlled Growth of Organic Semiconductor Films in liquid

By

Daniel Wainwright Shaw

Accepted in Partial Completion
Of the Requirements for the Degree
Master of Science

Moheb A. Ghali, Dean of the Graduate School

ADVISORY COMMITTEE

Chair, Dr. David Patrick

Dr. Steven Emory

Dr. Brad Johnson

MASTER'S THESIS

In presenting this thesis in partial fulfillment of the requirements for a master's degree at Western Washington University, I grant to Western Washington University the non-exclusive royalty-free right to archive, reproduce, distribute, and display the thesis in any and all forms, including electronic format, via any digital library mechanisms maintained by WWU.

I represent and warrant this is my original work, and does not infringe or violate any rights of others. I warrant that I have obtained written permissions from the owner of any third party copyrighted material included in these files.

I acknowledge that I retain ownership rights to the copyright of this work, including but not limited to the right to use all or part of this work in future works, such as articles or books.

Library users are granted permission for individual, research and non-commercial reproduction of this work for educational purposes only. Any further digital posting of this document requires specific permission from the author.

Any copying or publication of this thesis for commercial purposes, or for financial gain, is not allowed without my written permission.

Daniel Shaw

May, 2011

Controlled Growth of Organic Semiconductor Films in liquid

A Thesis

Presented to

The Faculty of

Western Washington University

In Partial Fulfillment

Of the Requirements for the Degree

MASTER OF SCIENCE

By

Daniel Wainwright Shaw

May, 2011

Abstract

Organic molecular crystalline (OMC) films are being investigated for use in a wide range of potential applications, from field effect transistors, to light-emitting diodes, and photovoltaic cells. The ultimate utility of OMC materials for such applications will depend on the degree and type of molecular order in deposited films, as well as the processing costs for preparing them. The goal of this thesis is to develop a method to produce high quality OMC thin films under ambient conditions, to characterize those films, and their growth kinetics. In particular, I will investigate OMC film growth by ambient axisymmetric spray method, a technique in which an organic semiconductor is sublimated into a carrier gas at ambient pressure and deposited onto a substrate coated with a thin liquid layer. I will examine the growth kinetics and morphologies of the resulting films. The results of this research will be an improved understanding of the growth of organic crystals in a thin film of liquid and the production of cheap organic semiconductor thin films.

Acknowledgements

I would like to acknowledge the help from my thesis advisor, Dr. David Patrick, for his wisdom, motivation and constant optimism on this project.

In addition I would like to thank Dr. Brad Johnson and Dr. Steven Emory for being part of my graduate committee.

I would also like to thank Kevin Bufkin, Cory Lund, Alexandr Baronov, and Chase Reinhart for their work on this project.

I must also thank Geoff Landis at the machine shop of Western Washington University for his manufacturing skill and expert advice.

Table of contents

List of figures and tables

Figure or table **page**

Table of commonly used variables and constants

Symbol	Comment	Value	References
m_1	Tetracene molecular mass	3.791×10^{-25} kg	
m_{gas}	Argon molecular mass	6.634×10^{-26} kg	
r_1	Tetracene molecular radius	4.151×10^{-10} m	[1]
Ω	Molecular volume of crystalline tetracene	0.299 nm^3	[2]
s_a	Molecular surface area of crystalline tetracene	0.48 nm^2	[3]
ρ_g	Argon density at P = 1.36×10^5 Pa, T = 373 K	1.75 kg m^{-3}	
γ	accommodation coefficient	0.91	
T	gas temperature	373 K	
k	Boltzmann's Constant	1.3806×10^{-23} J K^{-1}	
x	Mobility radius exponent	0.46	[4], [5]
D_f	Fractal dimension	1.78	
a	Nozzle radius	1.905×10^{-3} m	
μ	Ar hydrodynamic viscosity	2.22×10^{-5} N m^{-2} s	[6]
z^*	Nozzle – substrate distance	0.015 m	
L	Nozzle length	0.025 m	
α	Axisymmetric stagnation point flow constant		
Re	Reynolds number		
Sh	Sherwood number		
St	Stokes number		
s	Tetracene-solvent surface energy	J m^{-2}	
i^*, a^*	Critical nucleus size	molecules	
β	Mass transport efficiency scaling exponent		
U	Jet velocity	m s^{-1}	
C_{eq}	Saturation concentration of tetracene in bis(2-ethylhexyl)sebecate at room temperature	6.6×10^{-4} M	This work
D	Diffusion coefficient	m^2 s^{-1}	

[1] "The crystal and molecular structure of tetracene" ,J. M. Robertson, V. C. Sinclair and J. Trotter, Acta Cryst. (1961). 14, 697

[2] "The crystal and molecular structure of tetracene", Robertson, J. M.; Sinclair, V. C.; Trotter, J., Acta Cryst. 1961, 14, 697.
[3] "The crystal and molecular structure of tetracene", Robertson, J. M.; Sinclair, V. C.; Trotter, J., Acta Cryst. 1961, 14, 697.
[4] Cai, J. and Sorensen, C. M. (1994) Diffusion of fractal aggregates in the free molecular regime. Phys. Rev. E 50, 3397
[5] GM Wang, CM Sorensen, Diffusive Mobility of Fractal Aggregates over the Entire Knudsen Number Range, Physical Review E. 60 (1999) 3036-3044.
[6] Wilhelm, J.; Vogel, E., "Viscosity measurements on gaseous Argon, Krypton, and Propane", Int. J. Thermophys. 2000, 21, 301.

Chapter One

1.0 Introduction

For over 60 years inorganic semiconductors have been the dominant material choice for semiconductors in the electronics industry. Recently however, organic semiconductors have also begun to receive some attention because of their compatibility with low temperature deposition methods enabling the use of flexible substrates, their potential for lower cost processing, and their chemical „tuneablitiy".[1] This chapter will provide background on uses of organic semiconductors, their important physical properties, and a several methods for preparing them in thin film form. This will be followed by a discussion on the basics of growth kinetics and what constitutes an ideal organic semiconductor thin film.

Broadly speaking, there are two main types of organic semiconductors: organic molecular crystals (OMC) and conjugated polymers. OMC"s such as pentacene, which is one of the most widely studied OMCs, and rubrene, which has shown the highest mobility,[2] are easily sublimed and show electronic performance approaching those of amorphous silicon in some cases. The greatest challenge with OMC"s is their poor solubility.[3] This causes problems because solution-based processing methods such as spin coating are often among the least expensive ways to deposit thin films. Conjugated polymers such as polythiophene and poly(triarylamine) have higher solubilities and are therefore more readily processed in thin film form, but have problems achieving high enough charge carrier mobilities for many practical applications. [4,5,6,7,8]

The current generation of organic semiconductors has the potential to displace inorganic semiconductors in relatively low performance devices such as low cost solar cells[9] and switching circuitry in active matrix flat panel displays.[10] Recently, organic semiconductors have been demonstrated in organic light emitting diodes (OLEDs),[11,12] organic solar cells,[13,14,15] field effect transistors (OFETs),[16] radio frequency identification tags(ORFIDs),[17] and sensor arrays.[18] In 2008 Sony introduced the first industry OLED TV which was said at the time "will soon become the standard against which all TVs are measured."[19]

The primary advantage of organic semiconductors is their potential lower cost of production. Processing of traditional inorganic semiconductors requires complicated high-vacuum equipment and relatively high processing temperatures, all of which decreases manufacturing throughput and increases costs. The potential for lower production costs with organic semiconductors stems from the removal of the need for high vacuum and compatibility with lower processing temperatures. In addition, because organic semiconductors are molecular materials they are much more amenable to chemical modification for the engineering of more favorable electronic properties, or to add substituents to aid in processing such as patterning and solubility.[20,21]

1.1 Electronic Properties of Organic Semiconductors

In order to produce an effective organic semiconductor, knowledge of a few relevant physical properties is important. In this section, I will discuss charge transport, the importance of crystalinity, chemical impurities, anisotropic mobility, macroscopic orientation, and crystallite size.

Charge transport in inorganic semiconductors can be described by band theory. According to band theory filled and empty valence orbitals combine to form two wide energy bands, called conduction and valance bands. The conduction band is delocalized throughout the entire crystal, allowing charge carriers in the conduction band (electrons or holes) to move relatively freely. By contrast, charge carriers in the valence band are much more closely bound to individual atomic centers, and hence immobile.

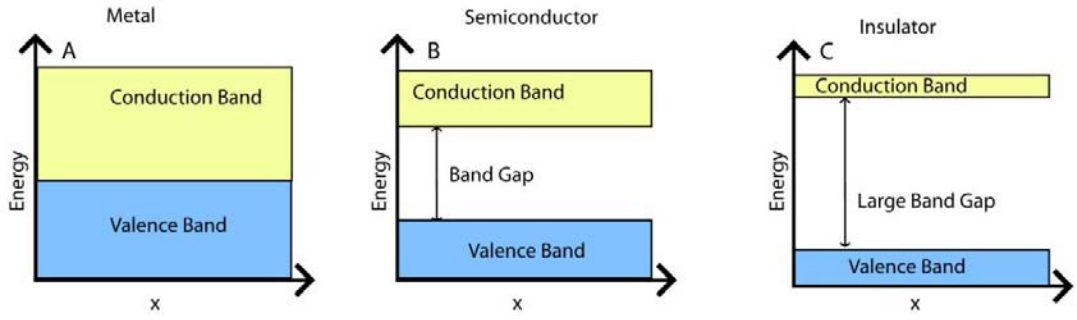

Figure 1.1
A) Valence and conduction bands of a metal. B) Valence and conduction bands of a semiconductor showing a small band gap. C) Valence and conduction bands of an insulator, note the large band gap.

As shown in figure 1.1, in a metal, the conduction and valance bands overlap allowing electrons to move relatively freely throughout the solid. In an insulator, the conduction and valance bands are far apart and electrons have a hard time jumping the gap of 3-4eV. In a semiconductor the gap between the conduction and valance bands is small, greater than zero but less than 3 or 4 eV[22]. For semiconductors and insulators this range of energies is called the band gap. The band gap energy region is forbidden and therefore in order for an electron to transition from the occupied valence band to the unoccupied conduction band it must be excited by a photon

capture, charge injection, or thermal excitation. When an electron is excited into the conduction band by one of these mechanisms it leaves behind a charge deficient „hole". In the absence of an external applied field the conduction electron and hole undergo random diffusive motion until eventually recombining, releasing energy equal to the band gap as shown schematically in figure 1.2 A. However when an electric field is applied, the valance and conduction energy bands are distorted, shown in figure 1.2 B, causing electrons and holes to move in opposite directions and producing a net flow of current. One important measure of the quality of semiconductor is its field effect charge carrier mobility (μ [$cm^2V^{-1}s^{-1}$]), the ratio of the velocity of the charge carrier to the magnitude of the applied electric field.

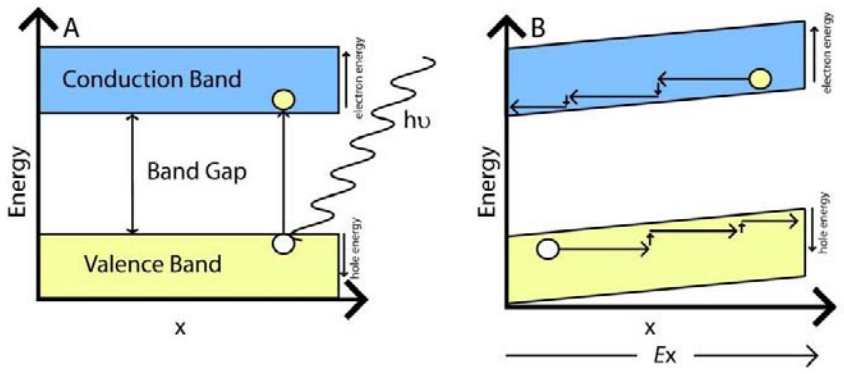

Figure 1.2
A) Delocalized band energy levels showing the excitation of an electron from the valence band to the conduction band. B) Movement of hole and electron under an applied field.

Unlike the covalent bonding network in an inorganic semiconductor, organic semiconductor molecules are often held together by weak van der Waals forces; because of this they do not form delocalized orbitals and do not exhibit the same kind of band structure. Charge transport in organic semiconductors occurs via a different

mechanism. There are two main contributors to charge carrier mobility in an organic semiconductor, summarized in equation 1

Equation 1

$$\mu_{tun} + \mu_{hop} = \mu$$

The total mobility can be expressed as a sum of two factors: a contribution from μ_{tun}, electron tunneling (coherent electron transfer), and from μ_{hop}, the contribution to the mobility via a hopping (incoherent electron transfer).[23] At low temperatures, μ_{tun} dominates and organic semiconductors behave more similarly to their inorganic counterparts, while at higher temperatures μ_{hop} dominates and a hopping mechanism better describes charge transfer. In the latter case an electron transitions, or „hops" from the highest occupied molecular orbital (HOMO) on one molecule over a potential barrier to the lowest unoccupied molecular orbital (LUMO) on a neighboring molecule. The hopping process may be assisted by lattice vibrations („phonon-assisted" hopping), or by relaxation of the local electrostatic field („polaron-assisted" hopping). In both cases the π conjugated system is primarily involved because of its ability to delocalize an acquired charge. The amount of π-π overlap between neighboring molecules largely determines the energy barrier size that the electron has to overcome.[21,24] Figure 1.3 A shows hopping events for an organic semiconductor under no applied field where charge migration is purely diffusive and there is no net current. Figure 1.3 B shows a similar organic semiconductor under an applied field. In this situation electrons tend to travel in a single direction while holes travel in the opposite direction, producing a net flow of current.

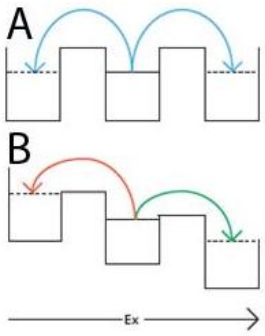

Figure 1.3
A) Charge carrier hopping events in an organic semiconductor under no electric field. B) Charge carrier hopping events in an organic semiconductor under an applied electric field adapted from [25]

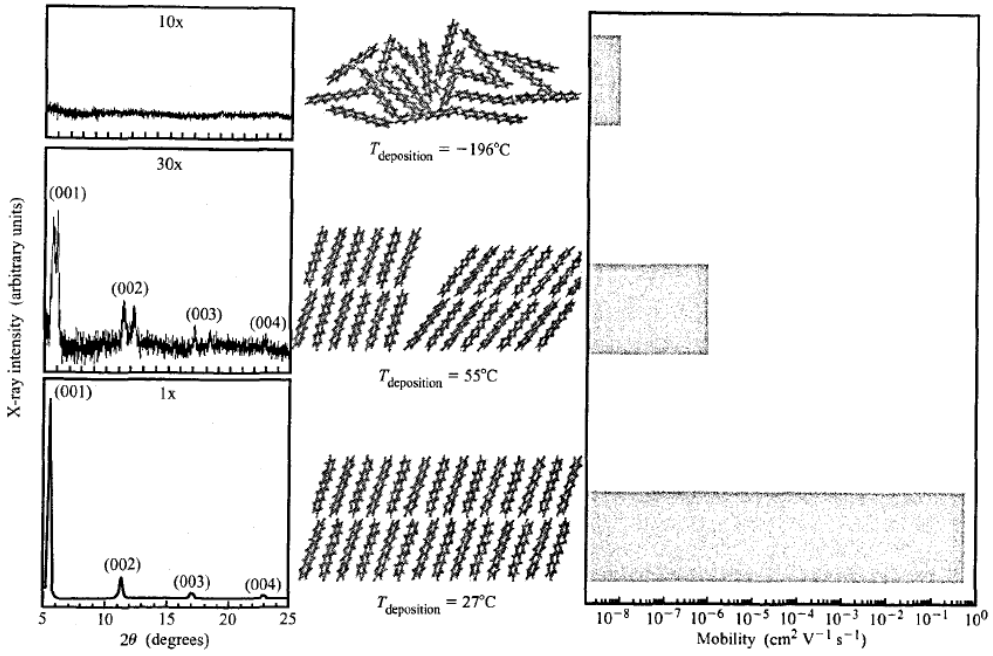

Figure 1.4
X-ray diffractograms of pentacene in various states of crystallographic order next to its cartoon representation and bar graph of mobilities of films of different crystallographic order. From [27]

Highly ordered molecular crystals with closely interacting conjugated π systems are usually associated with higher charge carrier mobilities, and much work has been done on introducing structural modifications to small-molecule organic semiconductors to improve the crystalline π-π overlap between neighboring molecules.[26] Due to the need for close π-π overlap between neighboring molecules, a well ordered densely packed crystal structure is required for high charge carrier mobility. This is illustrated in Figure 1.4 for the case of pentacene, where the charge carrier mobility was found to vary by about six orders of magnitude between amorphous, polycrystalline, and single crystal samples.[27] Thus in order to achieve the best performing devices, a high degree of molecular order is required.

Charge carrier mobility is also very sensitive to the presence of impurities, which are associated with four types of significant problems: deep traps, shallow traps, lattice distortions,[28] and scattering sites. Deep traps and shallow traps affect charge transport exactly as their name suggests, by trapping charge carriers and impeding them from moving and producing a current. The distinction between deep and shallow traps concerns the depth of the energy well; for deep traps the well depth is $>> k_BT$ whereas for shallow traps it is on the order of k_BT which allows for thermal detrapping. Deep traps reduce the overall population of free charge carriers thus reducing mobility. Shallow traps effectively reduce the speed at which charge carriers propagate. Impurities can be synthetic byproducts, or introduced during device fabrication. Usually they do not carry a permanent charge, but become charged when trapping an electron or hole. These point charges create lattice distortions which further impede charge mobility by acting as scattering sites for other charge

carriers.[23] As a result, high purity crystals are required to produce films with high charge carrier mobility.

Another important factor affecting organic semiconductor performance is crystallographic orientation. Figure 1.5 shows a single molecule of rubrene, an OMC with one of the highest known mobilities, as well as its crystal structure. Upon examination of the packing in the crystal structure one observes a greater degree of π-π overlap in the b-axis relative to the a-axis. Figure 1.6 presents a graph of the mobility of a rubrene single crystal measured along different crystallographic directions. As can be seen, the mobility parallel to the a-axis (0° to 90°) is 4.4 cm^2/Vs, while along the b-axis (180° to 360°) it is nearly four times larger at 15.4 cm^2/Vs.[29] The difference occurs as a result of the high degree of π-π overlap between neighboring molecules along the b-axis and relative lack of π-π interaction on the a-axis. This shows that the relative orientation of the different crystals that make up a thin film is important in producing high mobility thin films.

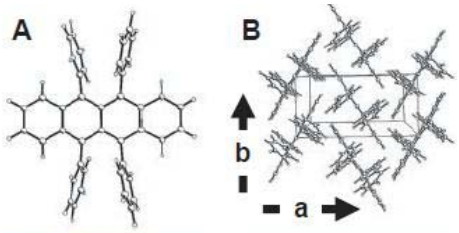

Figure 1.5
A) chemical structure of rubrene.
B)crystal structure of rubrene adapted from[29]

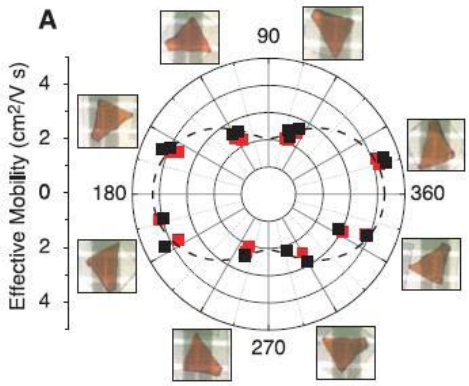

Figure 1.6
Mobility of a single crystal of rubrene along different crystallographic directions. From Ref. [29].

A final consideration in producing a high quality thin film devices is crystallite size. In figure 1.7, an AFM image of a pentacene thin film is shown.[30] As with most organic thin films, the one in figure 1.7 is made up of a large number of small (micron-sized) crystals. Each gap between the crystals presents an energy barrier impeding charge transport. Like a large number of resistors in series, the collective effect is to retard the flow of charge and lower the overall mobility of the film.

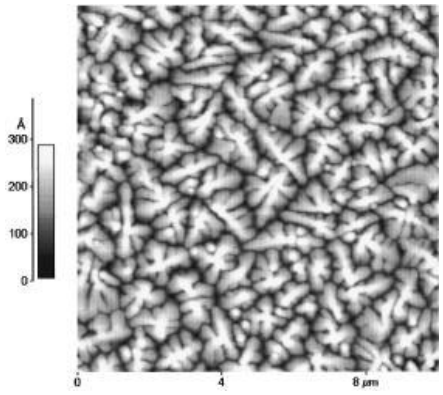

Figure 1.7
AFM image of pentacene thin film. From Ref. [30].

1.2 Film Growth Methods

This section will discuss some of the most common ways of producing organic semiconductor thin films. One method involves preparing a saturated solution of organic semiconductor and applying that solution to a substrate by spin or dip coating. The degree of super-saturation is then controlled via cooling the substrate, or evaporating the solvent to promote regulated nucleation.[31] Another similar solution processing method uses a crystal suspension of organic semiconductor crystals in a solvent. Evaporation of the solvent after the suspension has been spun or dip coated onto a substrate leaves behind a thin film of the suspended crystals.[32] These methods have proven promising for their ability to grow crystals with tunable morphology and high throughput possibilities but tend to produce lower quality organic semiconductor thin films because of problems with impurities introduced from the solution or from unwanted chemical reactions, as well as poor contact between crystals.

Another group of methods involves deposition via sublimation, done either under high vacuum directly on to a dry substrate[33] or into a thin liquid layer,[34] or under low vacuum in the presence of an inert carrier gas,[35] or at ambient pressure with an inert carrier gas.[36] In a method closely related to the work described in this thesis, Voigt *et al.* used a vapor phase deposition method under high vacuum to deposit sublimed tetracene into bis(2-ethylhexyl) sebacate continuously saturating the liquid thin film, and forcing the nucleation of crystals. This method produced crystals that were significantly larger than those typically grown on bare surfaces, but still required high vacuum conditions, which from a technological standpoint slows down throughput

and increases cost. Shrein *et al.,* introduced a significant improvement in which an organic source material is evaporated in a three-zone furnace used to establish a temperature gradient from the source material to the water cooled substrate. The source material is then carried by an inert gas to the substrate while the chamber is under low vacuum at pressures of 0.025-1.3 Torr. A schematic for this deposition method is shown in figure 1.8.[35] Sublimation under low vacuum with an inert carrier gas is slightly less expensive but still produces small crystals. Biswas *et al.*[36] demonstrated an effective method of printing molecular organic semiconductors on to a substrate at ambient pressures. In this method an organic semiconductor source is sublimed in to an inert carrier gas and that gas impinges as a collimated jet on to a cooled substrate where the organic semiconductor condenses. To prevent oxidative damage to the organic vapor an annular channel was used to create a guard jet of inert gas to provide a oxygen free environment for deposition to occur. A photograph and schematic of the nozzle is shown in figure 1.9.

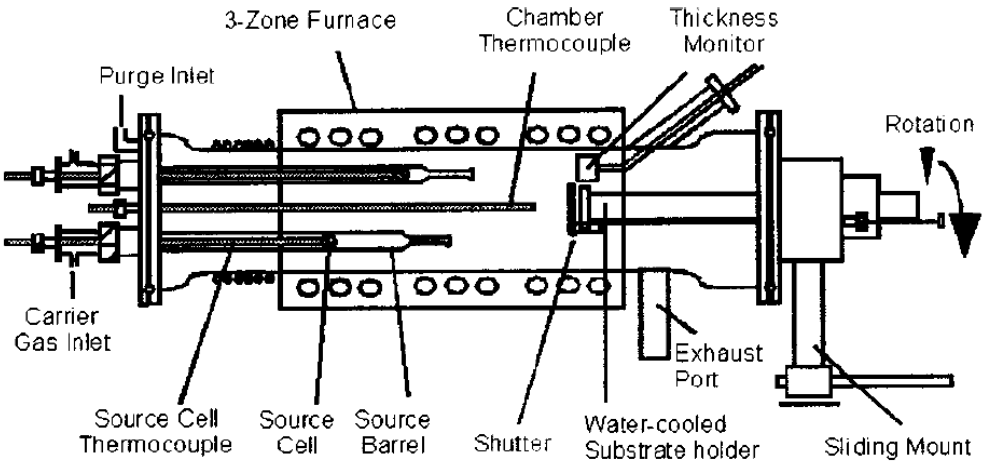

Figure 1.8
Schematic of low-pressure organic vapor phase deposition. From Ref. [35]

For practical applications, films must be patterned to define device elements, establish electrical connections, etc. Several patterning methods specific to organic semiconductors have been developed for both solution processing and vapor phase deposition. These include feature definition using self-assembled monolayers (SAM), photolithography, and physical masking.

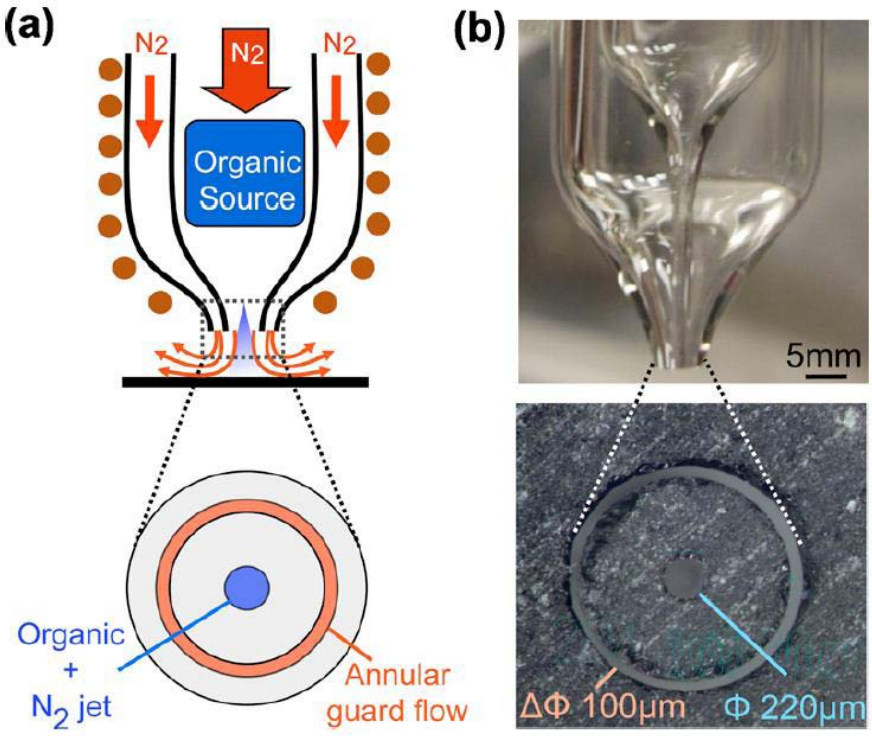

Figure 1.9
a) Schematic of heated nozzle with an annular guard flow channel to protect the organic vapor in the N_2 gas stream b) Photograph of nozzle not the small size which increases the resolution of patterning. From Ref. [36]

SAMs have been used in both solution and vapor phase deposition techniques. A microcontact printing technique,[37] shown in figure 1.10, is used to deposit an array of deposited SAMs which is used as a template to either promote or discourage

nucleation at specific surface site,[38] or to promote or discourage wetting patterns in solution processing.[39,40] In this microcontact printing technique, a SAM film is printed on to a substrate using an elastomeric stamp to define hydrophobic and hydrophilic regions, as shown in figure 1.10.

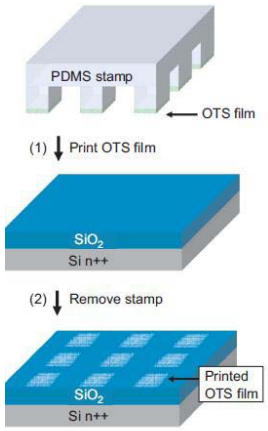

Figure 1.10
Schematic outline of a microcontact printing technique use to create an array of SAMs. A PDMS stamp is inked with octadecyltriethoxysilane (OTS) ,a type of SAM, then the stamp is brought in to physical contact with the substrate and left in contact for some time and when removed an array of SAMs has been deposited[41]

For films grown by vapor phase deposition, the SAM promotes nucleation and crystal growth from vapor phase deposition,[41] producing films with highly controlled deposition on just the hydrophobic regions. The method allows for spatial control, but no alignment control.

Ober *et. al*. have developed a dry photolithographic patterning process using supercritical carbon dioxide as a solvent. A general schematic of this process is shown in figure 1.11.[42] In this method a complete thin film is deposited and covered by photoresist. The pattern that is wanted is then exposed to UV light changing it from CO_2 philic to CO_2 phobic. The substrate is then treated with super critical CO_2

and then developed removing the semiconductor thin film layer that is not capped by CO_2 phobic photoresist. The photoresist is then removed in selected areas by exposure to UV light, leaving a patterned semiconductor layer in the unexposed regions. While high resolution is possible with this method, there are many steps involved, and the potential for introducing chemical impurities.

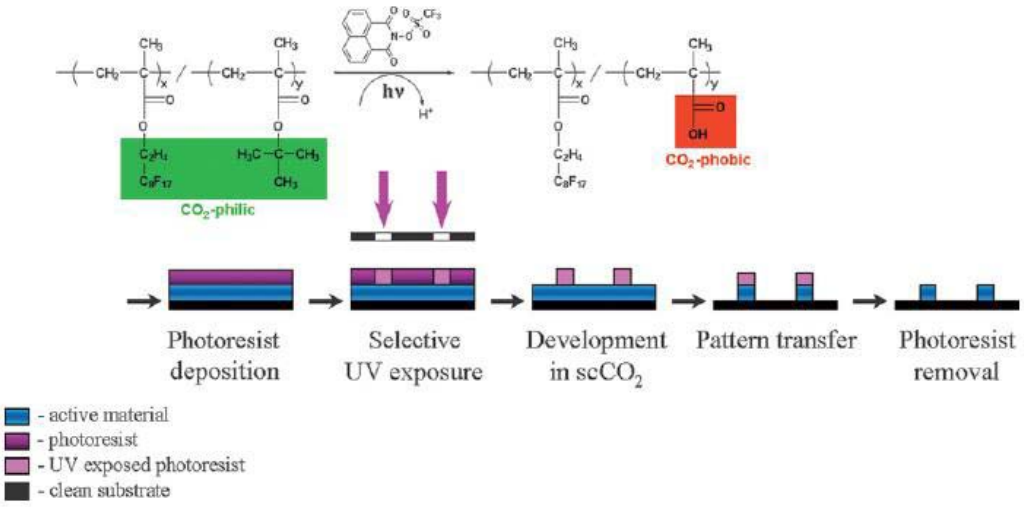

Figure 1.11
Schematic of dry photolithographic patterning adapted from[42]

One of the simplest ways to pattern a substrate is to simply mask off a negative image of the pattern you wish to produce with tape or some other solid easily removable substance. The whole substrate then has a thin film deposited on it and the mask is removed leaving the reverse pattern behind.[43] The advantages of masking are its simplicity, the fact that it works with all organic semiconductors, its compatibility with flexible substrates, and its ease of production on large area substrates. However, it has limited resolution.

As discussed previously in section 1.1, molecular and crystallographic order has a large effect on the performance of an organic semiconductor thin film. For this reason many different ways of aligning thin films have been devised including: mechanical stretching,[44] frictional transfer,[45] rubbing,[46] zone casting [47] and the use of liquid crystals.[51] In the mechanical stretching technique an organic thin film on a flexible substrate is physically stretched, elongating one axis and encouraging polymer chains to orient in one direction adding macroscopic order to the thin film.[44] This simple technique only works with polymer organic semiconductor thin films and only on stretchable substrates. The friction-transfer method involves using a teflon rod or other similar material that is dragged across a surface, leaving behind a thin oriented polymer layer. When an organic semiconductor is deposited on this layer, growth is promoted along one crystallographic direction.[45] In a related method, a photosensitive polymer precursor layer is exposed to linearly-polarized UV light, causing preferential crosslinking to occur along the polarization direction, increasing the probability of polymer main-chains aligned in the direction parallel or perpendicular to the polarization direction, depending on the alignment layer used.[48] Previously this technique has been used to align liquid crystalline materials.[45,49,50] In the zone casting method a solution is spread by means of a nozzle onto a moving substrate. The substrate and nozzle are carefully thermally controlled in order to promote specific evaporation rates. Under these conditions a stationary gradient of concentration is formed within the meniscus producing directional crystallization. A schematic of this method is shown in figure 1.12**.**

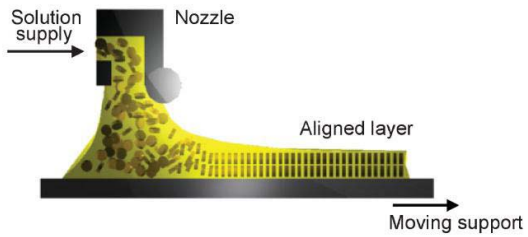

Figure 1.12
Zone casting method schematic. From Ref. [47]

This thesis builds on work by previous group members. It is closely related to method developed by Wilkinson *et. al.* [51] called organic vapor liquid solid (OVLS) deposition, which uses vapor-phase deposition into a thin thermotropic liquid crystal layer. In this technique a liquid crystal layer is spin coated on to an orienting polyimide surface and an organic vapor generated by sublimation near atmospheric pressure is deposited on the substrate. The main difference between OVLS and Shrein *et. al.'s* method is the liquid crystal layer and use of near-ambient pressures. The thesis also builds on the method developed by Bufkin *et. al.* which is introduced a carrier gas to accelerate the rate of vapor deposition. Because the gas impinges on the substrate with an axisymmetric stagnation point flow, it was dubbed ambient axisymmetric spray (AAS).[25]

1.3 Thesis Goals

The goals of this thesis are to introduce improvements to the methods of Bufkin and Wilkinson leading to better reproducibility and film quality through the use of a redesigned experimental apparatus, to characterize the hydrodynamics and gas-phase kinetics of particle aggregation and deposition, and to use the improved method in

studies of the growth kinetics, structural, chemical, and electronic properties of organic semiconductor films on liquid covered and bare substrates.

---

[1] Shuhong Liu, Wechung Maria Wang, Alejandro L. Briseno, Stefan C. B. Mannsfeld, Zhenan Bao, *Adv. Mater.* **2009**, 21, 1-16

[2] J. Takeya, M. Yamagishi, Y. Tominari, R. Hirahara, Y. Nakazawa, T. Nishikawa, T. Kawase, T. Shimoda, S. Ogawa, appl. Phys. Let. **2007**, 90, 102120

[3] Yanming Sun, Yunqi Liu ,Daoben Zhu *J. Mater. Chem.* **2005, 15,** 53

[4] Günes, S.; Neugebauer, H. Chem. Rev. **2007,** *107*, 1324

[5] Jenekhe, S. *Macromolecules* **2001,** *34,* 7315

[6] S. Hotta and K. Waragai, J. Mater. Chem., **1991**, 1, 835.

[7] F. Garnier, A. Yassa, R. Hajlaoui, G. Horowitz, F. Deloffre, B. Servet, S. Ries and P. Alnot, J. Am. Chem. Soc., **1993**, 115, 8716

[8] Ahles M. Appl. Phys. Lett., **2004**, *84*, 428

[9] Chiatzun Goh, Michael D. McGehee, Nat. Acad. Eng. : the bridge **2005** 35, 4

[10] Amanda R. Murphy, Jean M. J. Frechet, Chem. Rev. **2007,** 107, 1066

[11] H. Burroughes, C. Bradley, R. Brown, N. Marks, K. Mackey, H. Friend, L. Burns, B. Holmes, *Nature* **1990**, 347, 539-541

[12] S. Sepeai, M. M. Salleh, M. Yahaya, A. A. Umar, *Thin Solid Films* **2009**, 517, 4679-4683

[13] P. F. Baude, D. A. Ender, M. A. Haase, T. W. Kelley, D. V. Mures, S. D. Theiss, *Appl. Phys. Lett.* **2003**, 82, 3964

[14] **A.** Macros Ramos, M. T. Rispens, J.C. Hummelen,R. A. J. Jansen, *Synth. Met.* **2001**, 119, 171

[15] J. M. Leger, D. G. Patel, D. B. Rodovsky, G. P. Bartholomew, *Adv. Funct. Mat.* **2008**, 18, 1212

[16] M. Sonntag, K. Kreger,D. Hanft, P. Strohriegl, *Chem. Mater.* 2005,17, 3031-3039

[17] R. Rotzoll, S. Mohapatra, V. Olariu, R. Wenz, M. Grigas, K. Dimmler, O. Shchekin, A. Dodabalapur, *Appl. Phys. Lett.* **2006**, 88 123502

[18] B. Crone, A. Dodabalapur, A. Gelperin, L. Torsi, H. E. Katz, A. J. Lovinger, and Z. Bao, *Appl. Phys. Lett.* **2001,** 78, 2229

[19] http://news.sel.sony.com/en/press_room/consumer/television/release/32499.html

[20] A. Afali, C. D. Dimitrakopoulos, T. O. Graham, *Adv. Mater*. **2003**, 15, 2066

[21] Zhihua Chen, Peter Muller, and Timothy M. Swager, Org. Lett., **2006,** 8, 2, 273

[22] Joel I. Gersten, Frederick W. Smith *The physics and chemistry of materials, :*wiley: new York, **2001**

[23] Veaceslav Coropceanu, Je´roˆme Cornil, Demetrio A. da Silva Filho, Yoann Olivier, Robert Silbey, Jean-Luc Bre´das Chem. Rev. **2007,** 107, 926-952

[24] Swenberg, C. E.; Pope, M. *Electronic Processes of Organic Crystals and Polymers*; Oxford University Press: Oxford, NY, 1999.

[25] Kevin Bufkin, MS thesis, Western Washington University, Bellingham, WA, 2010

[26] Zhihua Chen, Peter Muller, and Timothy M. Swager, organic Lett., **2006,** 8, 2, 273

[27] C. D. Dimitrakopoulos and D. J. Mascaro, *IBM J. Res. Devel*. **2001**, 45, 11.

[28] T.P. Nguyen, *Mat. Sci. in Sem. Process.*, **2006**, 9, 1-3

[29]Vikram C. sundar, ,Scince **2004,** 303,1644

[30] Gundlach, *Appl.Phys. Lett.* **1999** 74. 3302

[31] Peter T. Herwig and Klaus Müllen, Adv. Mater. **1999**, 11, 6, 480

[32] S. H. Liu, W. C. M. Wang, S. C. B.Mannsfeld, J. Locklin, P. Erk, M. Gomez F. Richter, Z. N. Bao, Langmuir **2007**, 23, 7428

[33] Sirapat Pratontep , Martin Brinkmann, Frank Nu¨esch , Libero Zuppiroli, PHYS. REV. B **2004,** 69, 165201

[34] M. Voigt, S. Dorsfeld, A. Volz, M. Sokolowski, phys. Rev. let. **2003**, 91, 026103

[35] Max Shtein , Herman F. Gossenberger, Jay B. Benziger, Stephen R. Forrest ,J. Appl. Phys., 2001 89, 2, 1470

[36] Shaurjo Biswas, Kevin P. Pipe, Max Shtein, appl. Phy. Lett. **2010,** 96,263301

[37] Y. N. Xia, M. Mrksich, E. Kim, G. M. Whitesides, J. Am. Chem. Soc. **1995,** 117, 9576.

[38] A. L. Briseno, J. Aizenberg, Y. J. Han, R. A. Penkala, H. Moon, A. J. Lovinger, C. Kloc, Z. A. Bao, J. Am. Chem. Soc. **2005**, 127, 12164.

[39] A. L. Briseno, M. Roberts, M. M. Ling, H. Moon, E. J. Nemanick, Z. N. Bao, J. Am. Chem. Soc. **2006**, 128, 3880.

[40] S. C. B. Mannsfeld, A. Sharei, S. Liu, M. E. Roberts, Z. Bao, Adv. Mater **2008**, 20, 4044.

[41] A. L. Briseno, S. C. B. Mannsfeld, M. M. Ling, S. H. Liu, R. J. Tseng, C. Reese, M. E. Roberts, Y. Yang, F. Wudl, Z. N. Bao, Nature **2006**, 444, 913

[42] Ha Soo Hwang, Alexander A. Zakhidov, Jin-Kyun Lee, Xavier Andre, John A. DeFranco,Hon Hang Fong, Andrew B. Holmes, George G. Malliaras, Christopher K. Ober, J. Mater. Chem. **2008,** 18,3087

[43] Max Shtein, Peter Peumans, Jay B. Benziger, Stephen R. Forrest, J. Appl. Phys.,**2003**. 93, 4005

[44] G. Gustafsson, O. Inganas, H. Stubb, Solid State Commun. **1990**, 76,203

[45] J.C. Wittmann, P. Smith, Nature **1991**, 352, 414.

[46] M. Prelipceanu, O. G. Tudose, O. S. Prelipceanu, S. Schrader, K. Grytsenko, Mater. Sci. Semicond. Proc. **2007,** 10, 24

[47] W. pisula, A. Menon, M. Stepputat, I. Lieberwirth, U. Kolb, A. Tracz, H. Sirringhaus, T. Pakula, K. Mullen, Adv. Mater. **2005,** 17, 684.

[48] M. Nishikawa, B. Taheri, and J. L. West, Appl. Phys. Lett., **1998**, 72, 2403 1998

[49] J. H. Kim, Y. Shi, S. Kumar, S. D. Lee, Appl. Phys. Lett. **1997**, 71, 3162.

[50] M. Schadt, K. Schmitt, V. Kozinkov, V. Chigrinov, Jpn. J. Appl. Phys. Part 1, **1992**, 31, 2155.

[51] F. Scott Wilkinson, Ronald F. Norwood, Joseph M. McLellan, L. Rhys Lawson, and David L. Patrick J. AM. CHEM. SOC. **2006**, 128, 16468-16469

Chapter Two

2.0 Introduction

In this chapter a summary of previous Patrick group members work will be presented followed by a discussion of some of the advantages and disadvantages of others methods compared to the method presented in this thesis. A detailed description of the apparatus and experimental conditions will be presented, along with a summary of the results of the experiments carried out for this thesis on general film growth characterization and hydrodynamics.

Previous work in the Patrick group on this project was performed by two main contributors, F. S. Wilkinson and K. Bufkin. Wilkinson used an apparatus similar to the one described in this thesis as well as an analogous method for the production of a uniform liquid layer to control organic semiconductor growth and a method for removing the liquid layer after deposition without disturbing the organic semiconductor thin film. Wilkinson's method utilized a graphite crucible heated using a custom-built ceramic enclosure with nichrome wire heating element, subliming the organic semiconductor at ambient pressure. The substrate was then held upside-down directly over the graphite crucible and the organic semiconductor diffused to the liquid layer on the substrate dissolved, and nucleated large crystals. Some examples of this growth in various solvents are shown in figure 2.1. Wilkinson's method resulted in aligned films with large crystal sizes at ambient

pressure, but deposition was very slow which is not ideal for high throughput applications.

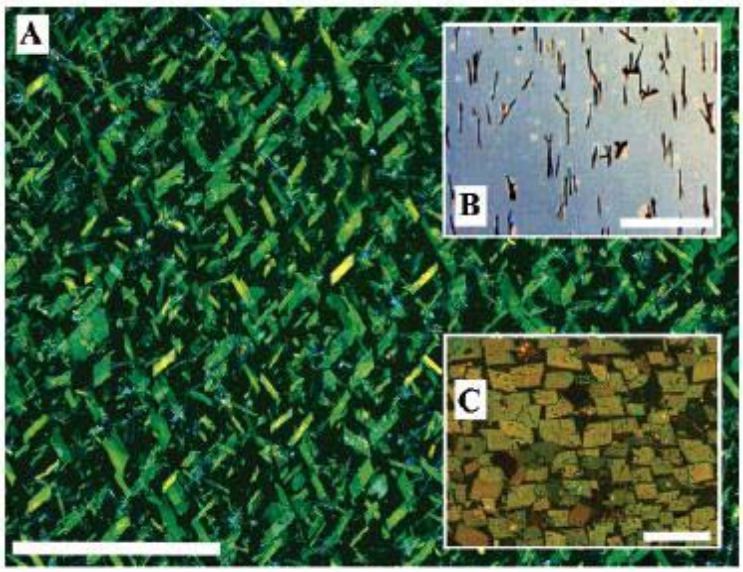

Figure 2.1
Scale bars are 100µm, tetracene thin films grown with three liquid crystal solvents: A) ZLI 3417 B) E7 C) MBBA. From Ref. [1].

Bufkin developed a method called ambient axisymmetric spray deposition (AAS). The main difference between AAS and Wilkinson's method is the addition of an inert carrier gas. In Bufkin's method a graphite crucible was heated to sublime an organic semiconductor (tetracene) while an inert carrier gas passed above the crucible carrying the vapor toward the substrate. The flow geometry created an axisymmetric stagnation point where the gas impinged on the substrate. A representative film grown by this method is shown in figure 2.2.

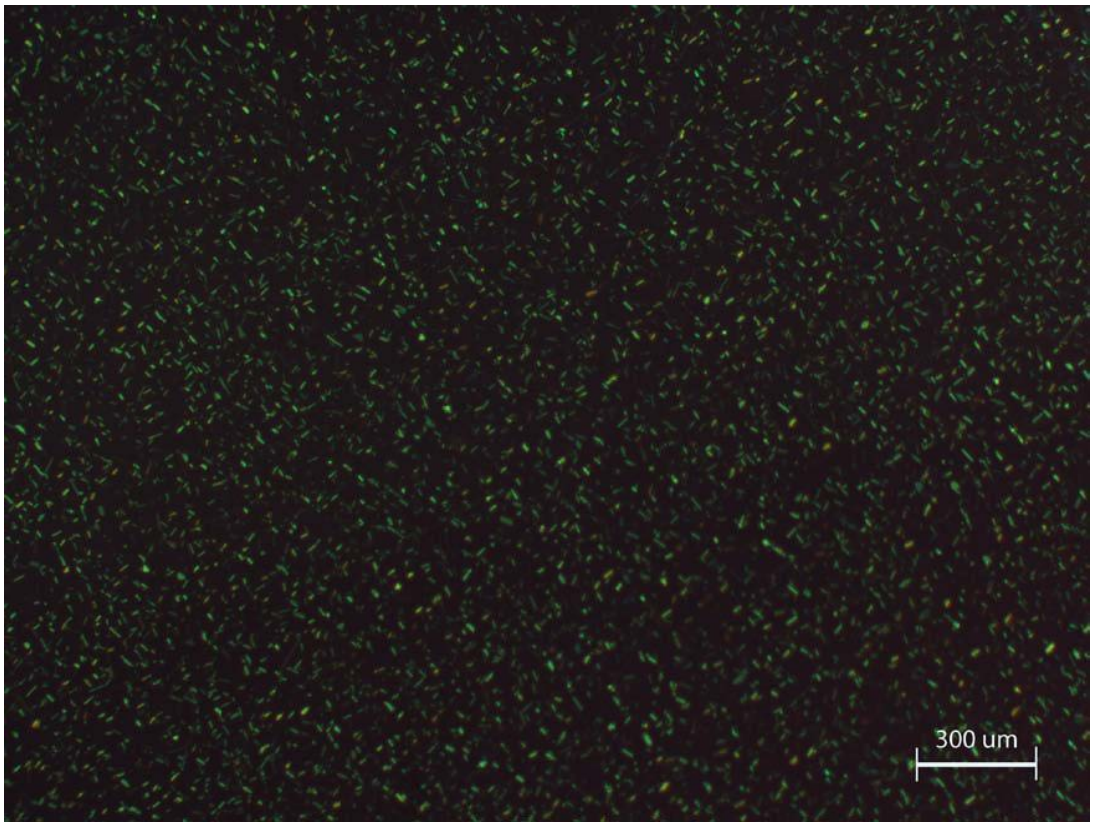

Figure 2.2
Representative film grown by Kevin Bufkin's AAS method. From Ref. [2].

Both methods work near ambient pressure, potentially reducing cost and complexity while increasing throughput. Working at ambient temperature enables compatibility with most substrates, including plastics. The liquid layer allows tuning of crystal growth, orientation, and has the potential to increase the chemical purity of deposited films. Working at ambient pressure does have its disadvantages however, for example vaporized organic semiconductor molecules follow diffusive trajectories, leading to the formation of vapor phase aggregates which may not fully dissolve upon reaching the liquid-coated substrate. Another limitation is reduced spatial resolution

due to the relatively long diffusion length of solute molecules in the liquid layer compared to adsorbates on a bare substrate. This ultimately limits the minimum size scale in devices incorporating patterned thin films.

2.1 Chamber Design

Building from the method and chamber design of Wilkinson and Bufkin the author introduced a modified deposition apparatus, shown in figure 2.3. The apparatus consists of four main regions: a heated crucible where sublimation occurs, a small mixing region where sublimate is diluted with a large volume of carrier gas, a needle directing gas flow to the substrate, and the substrate itself, where deposition occurs.

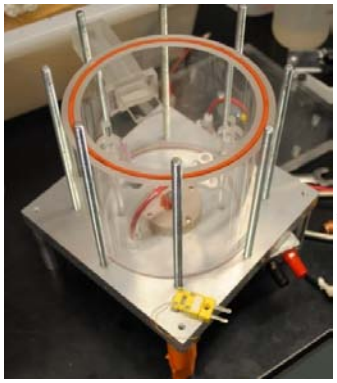

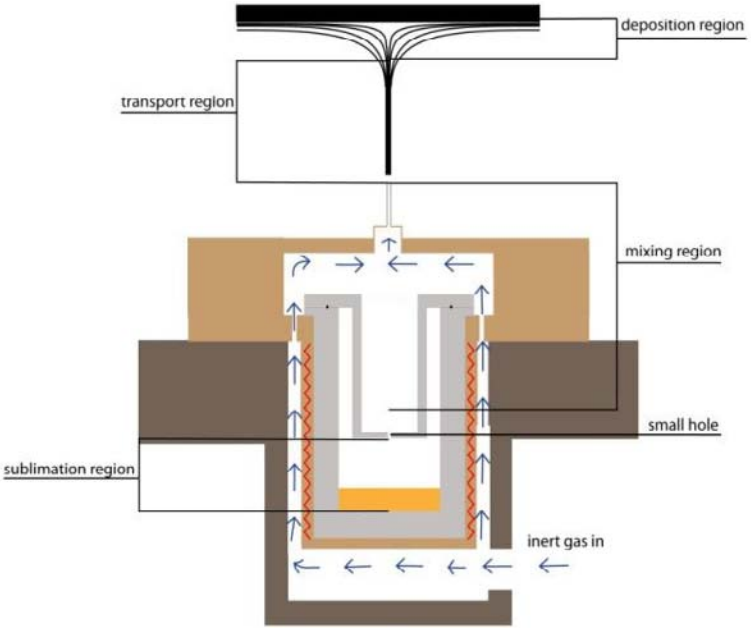

Figure 2.3
A photograph of the deposition apparatus and schematic showing the principle regions.

A schematic of the crucible along with a photograph of the source cell is shown in figure 2.4. The aluminum source cell is sealed with a Kalrez© O-ring and has a small opening with a diameter of 0.343 mm out of which vapor can escape. The temperature of the heating element used to sublime the tetracene is monitored and regulated via a built in thermocouple. The fluence of vapor through the opening depends on the partial pressure of sublimate in the crucible and the size of the opening.

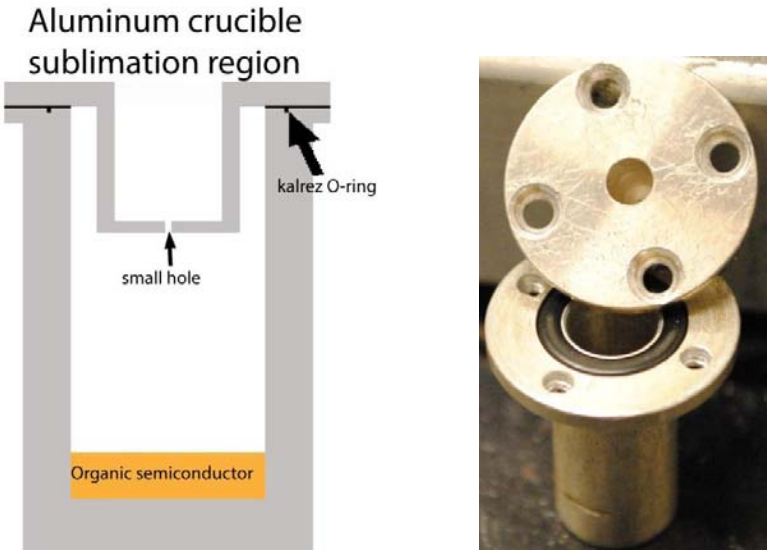

Figure 2.4
Schematic and photo of source cell/sublimation region

If the opening is very small and the sublimation rate is high enough, then the partial pressure within the crucible is not significantly affected by the loss of mass through the opening and a constant, time-independent fluence can be achieved. In this limit, such a source behaves as a Knudsen cell with the fluence depending only on temperature and not on the amount of solid material remaining in the crucible.

Although the size of the opening used in the source cell was much larger than the mean free path of molecules in the vapor phase, we found that the sublimation rate was indeed approximately independent of the mass loading for masses larger than 15 mg, as shown in figure 2.5. As a result, the cell could be used to deliver a constant concentration of gas phase tetracene which remained steady over a period of many hours.

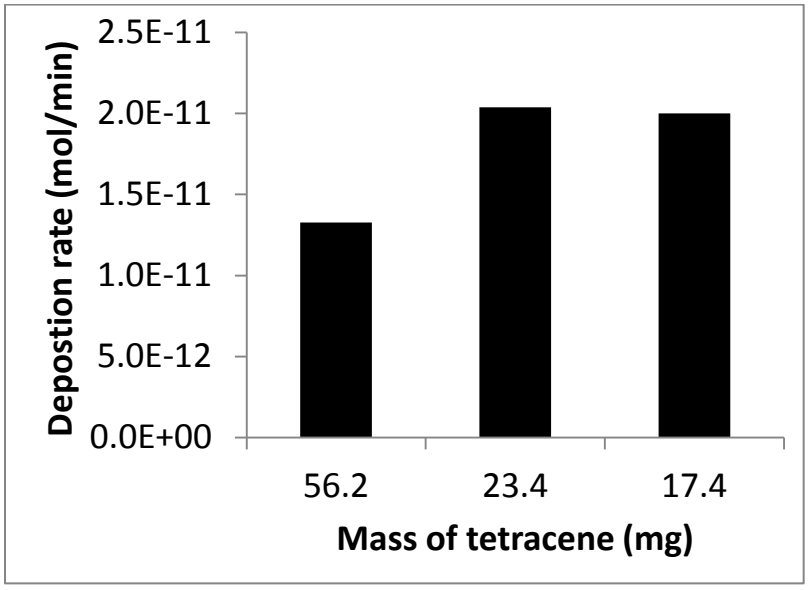

Figure 2.5
Deposition rate for various different masses of tetracene in source cell during deposition. Note that deposition rate is relatively independent of mass of tetracene added to the source cell

To find the dependence of deposition rate on the temperature of the crucible a series of experiments was conducted. To determine deposition rate as a function of temperature, thin films of tetracene were deposited on bare 1cm^2 ITO glass slides.

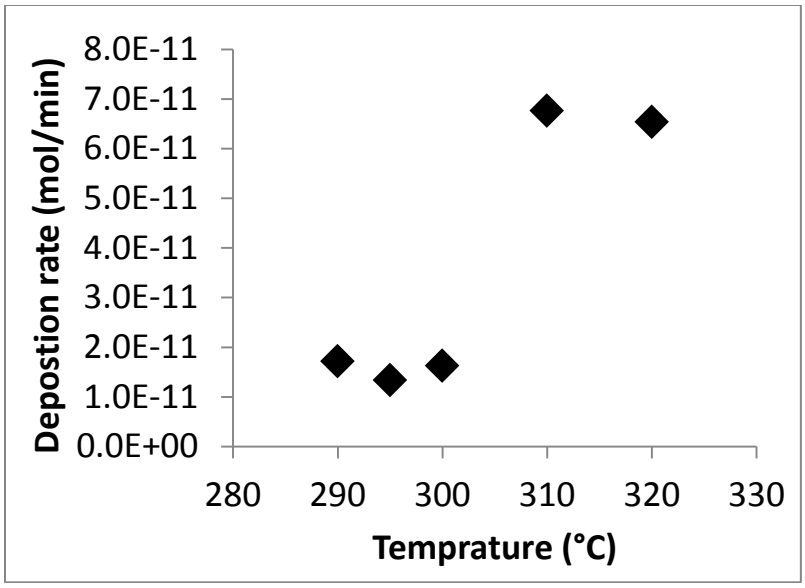

Figure 2.6
Deposition rate vs. crucible temperature. The runs used to produce this plot used a needle with an inner radius of 0.419 mm and a flow rate of 128ml/min

After deposition the slides were immersed in a known amount of hexanes and sonicated for one hour. UV-Vis spectra were then taken of the resulting hexanes mixture and the amount of tetracene was quantified from the absorbance at λ=274nm. The resulting dependence of deposition rate on crucible temperature is shown in figure 2.6. Directly above the source cell is a region where heated argon gas is introduced (figure 2.7).

The gas circulates over the top of the source cell, carrying sublimed material into the needle. The gas is not heated in this region and so the temperature begins to gradually decrease outside the crucible. To characterize the temperature profile, a series of measurements were made at different positions. Some of this data is shown

in figure 2.8. Under typical operating conditions, the temperature of the gas stream averaged about 100 °C.

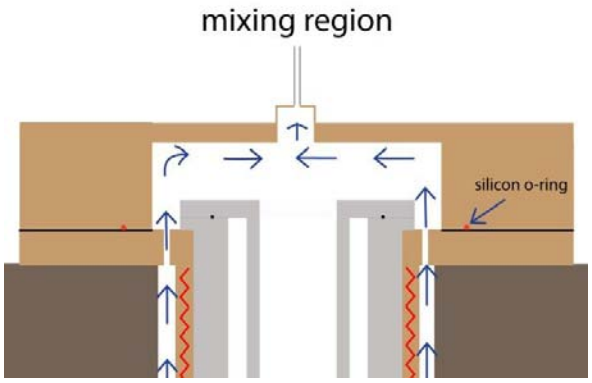

Figure 2.7
Schematic of the mixing region showing gas flowing over the source cell and up through the Luer Lok fitting and the needle

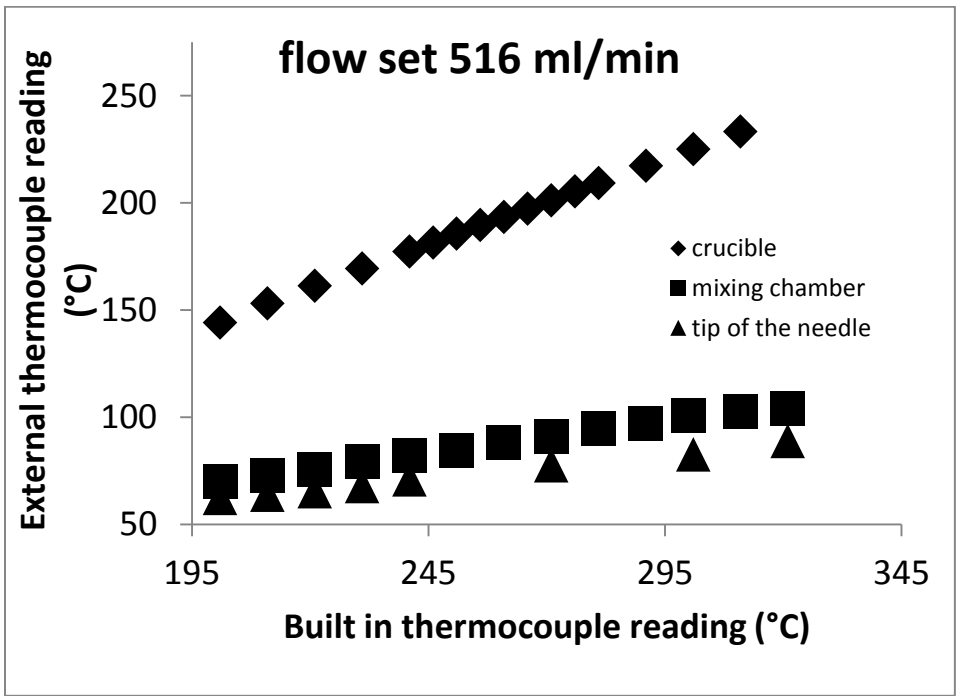

Figure 2.8
Temperature of different regions in the chamber measured with a secondary thermocouple plotted against the built in heating element thermocouple reading used to monitor and regulate heating element temperature.

2.2 Flow Calculations

[Portions of this section are based on a manuscript in preparation by Shaw, D., Bufkin, K., Lund, C., Baranov, A., and Patrick D.L.]

The flow of gas in the chamber was calculated in the following manner. First, the flow out of the chamber was measured with a He flow meter at various readings on the ball flow meter at the end of the chamber assembly, shown in figure 2.9. Then the He flow meter was calibrated at various flow rates by timing how long it took to displace 2L of water from a graduated cylinder at a given flow, shown in figure 2.10. A plot of the final calibration correlating the ball flow meters read out to the actual flow of gas out the exit of the chamber.

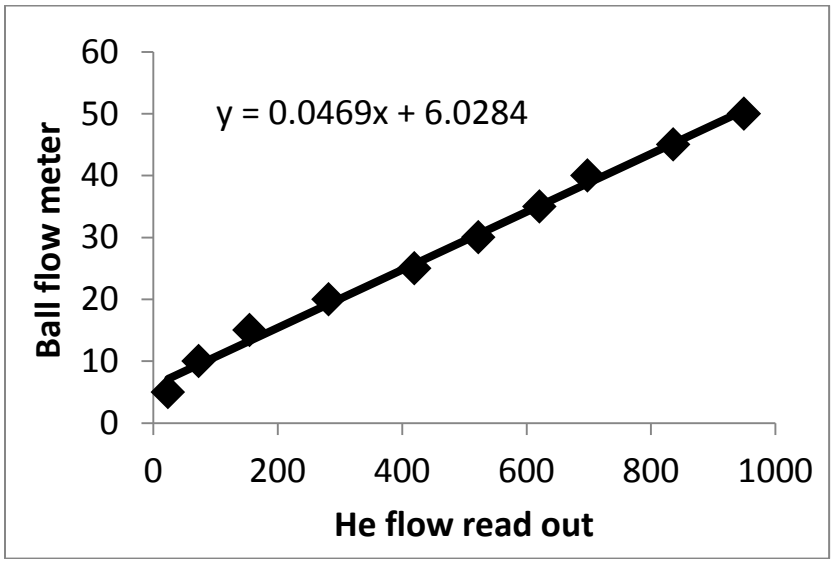

Figure 2.9
Ar flow out the exit of the chamber calibrated with a He flow meter.

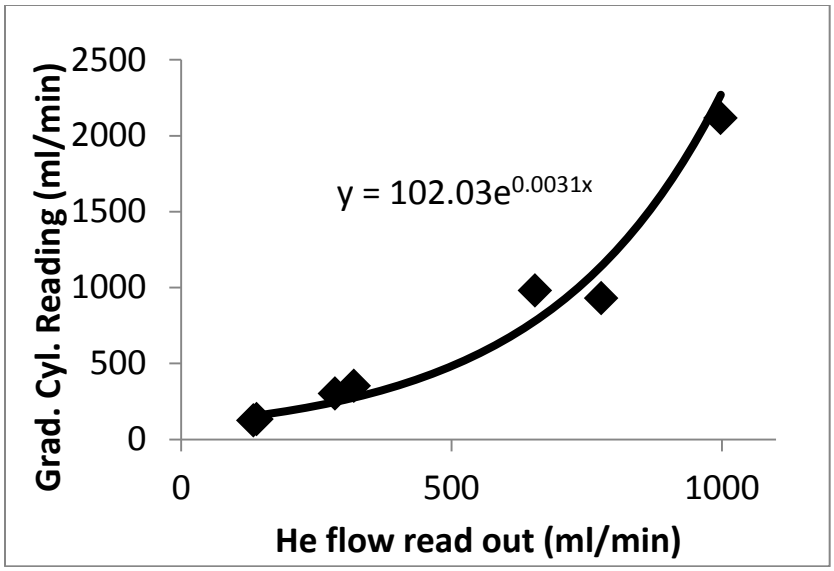

Figure 2.10
He flow meter calibration with displacement of 2L of water out of a graduated cylinder

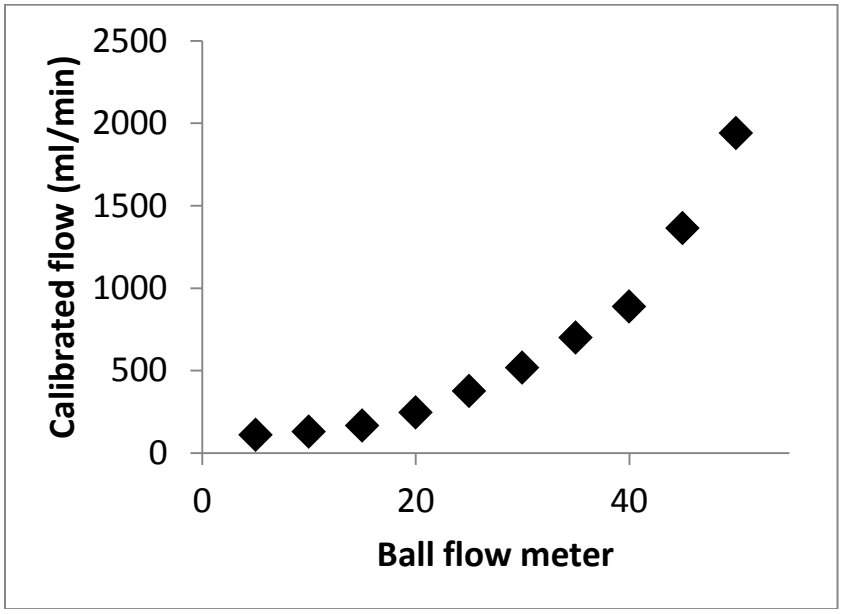

Figure 2.11
Flow calibration for ball flow meter vs. actual ml/min. Ball flow meter values have no units they are an arbitrary number taken off of a ball flow meter connected to the end of the apparatus.

Based on conservation of mass, the gas velocity at the base of the nozzle v_i can be computed as follows: Since the volumetric flow of gas out the end of the chamber, f_{vol}^{exit} has been measured, and the pressure at the end of the chamber is $P_{exit} = 1\ atm$, the mass of Ar per unit time flowing through the apparatus (and hence through the needle) can be found: $m = \rho_{exit} f_{vol}^{exit}$, where ρ_{exit} is the density of Ar at 1 atm. By conservation of mass, $\rho_i v_i \pi r \alpha^2 = m = \rho_{exit} f_{vol}^{exit}$, where α is the needle radius, and ρ_i is the density of Ar at the needle inlet pressure P_i and temperature T_i. We take the pressure P_i to equal the pressure at the regulator (5 psi above atmospheric pressure). The density of Ar at the base of the needle is given by $\rho_i = \frac{\rho_{exit} P_i T_{exit}}{P_{exit} T_i}$. As noted in figure 2.8 there is a small temperature gradient between the mixing chamber and the tip of the needle. To simplify the calculation, here we use the average temperature. Combining these equations gives:

$$v_i = \frac{T_i P_{exit} f_{vol}^{exit}}{T_{exit} P_i \pi \alpha^2}$$

Where:

P_{exit} =1.01x10^5 N m^{-2} is atmospheric pressure

P_i 1 atm + 5 PSI = 1.39 x 10^5 Nm^{-2}

T_i ≈373 K is the gas temperature in the needle

T_{exit} =300 K is the gas temperature at the end of the apparatus

Figure 2.12 shows the gas velocity at the base of the needle for the two needle diameters used in most experiments. Under typical experimental conditions the velocity was about 1 m s^{-1}.

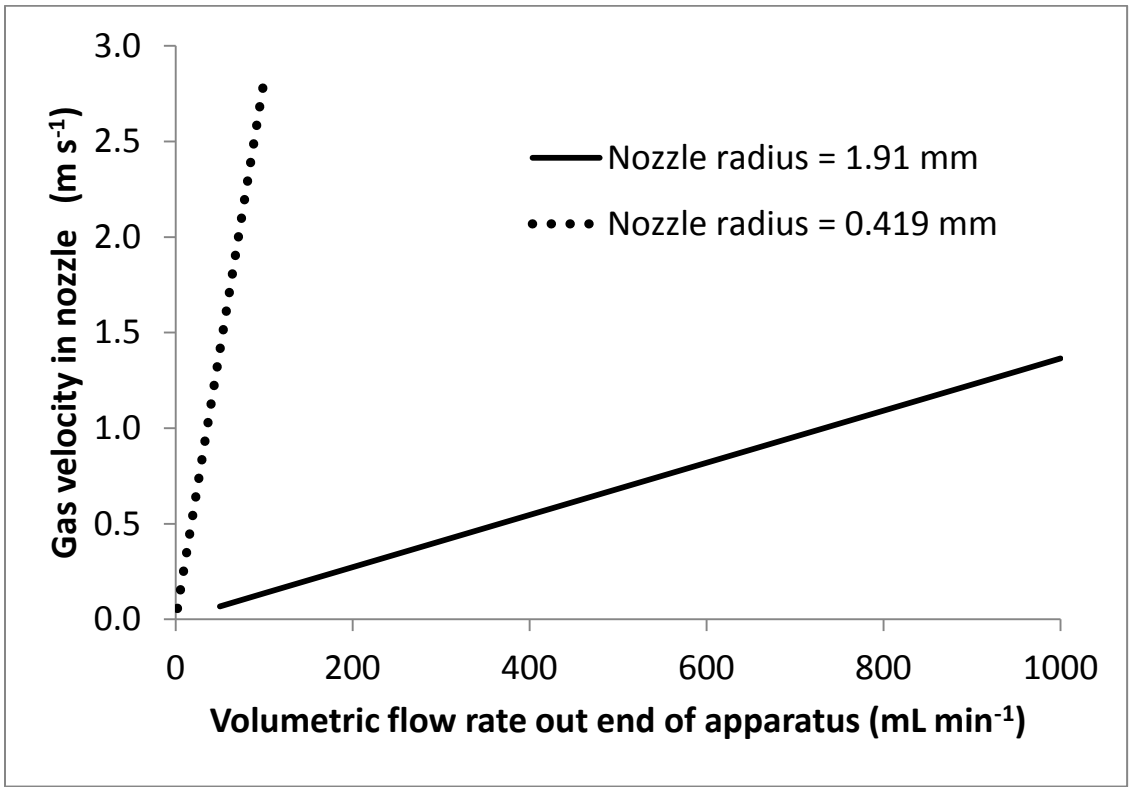

Figure 2.12
Relationship between the jet velocity and the volumetric flow rate for two needle sizes.

Approximating gas flow in the needle as compressible and isothermal, Poiseuille's equation for the pressure drop for fluid flowing in a frictionless pipe is $v_o P_o \pi\alpha^2 = \frac{\pi r^4}{16\mu L}(P_i^2 - P_o^2)$, where L is the length of the needle. From conservation of mass $v_o \rho_o \pi\alpha^2 = v_i \rho_i \pi\alpha^2$. For an ideal gas, $\rho_x \sim P_x$, so this equation can be re-written in terms of pressures as $v_o P_o = v_i P_i$, assuming isothermal conditions. This gives two

equations and two unknowns. Solving simultaneously yields: $P_o^2 = P_i^2 - \frac{16\mu L \nu_i}{r^2} P_i$. For the values of the variables used in the experiment we find $P_o \approx P_i$, in other words, there is no significant pressure drop along the length of the needle. Having computed the needle outlet pressure the radially averaged needle outlet gas velocity can be found from $\nu_o \rho_o \pi \alpha^2 = \nu_i \rho_i \pi \alpha^2$. Since $P_o \approx P_i$, we have $\nu_o \approx \nu_i$. The Reynolds number at the outlet of the needle is $Re = \frac{2\nu a \rho}{\mu}$, where ν is the gas velocity, α is the needle radius, ρ is the gas density at the pressure and temperature of the needle outlet and μ is the gas dynamic viscosity. For the range of experimentally-used flow rates and needle diameters, this works out to be Re = 20 ~ 400. Since this is much less than the onset value for turbulent flow in a pipe ($Re \leq$ ~2000), thus flow inside the needle is laminar. In the deposition region, the flux of sublimate to the substrate is determined by hydrodynamics. The laminar flow of gas on to a plate forms a static boundary layer[3]. This static boundary layer is a layer of gas right next to the substrate with zero velocity in the z direction towards the substrate. This provides a filtering effect where any material has to diffuse across this static boundary layer in order to be deposited on the substrate. A schematic of the deposition region is shown in figure 2.13. The hydrodynamics and static boundary layer in the system will be discussed more in depth in chapter 3.

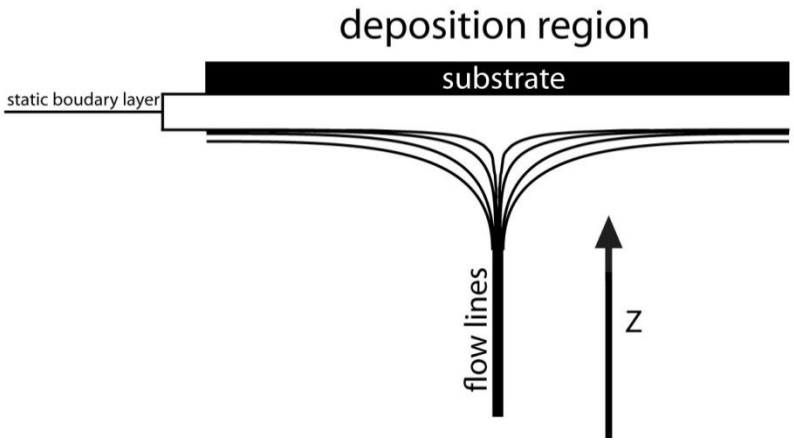

Figure 2.13
Schematic of the deposition region and static boundary layer

2.3 Substrate Preparation

Five different substrates were investigated, glass with a thin film of 2,2' thiodiethanol, indium tin oxide coated glass(ITO), ITO with a 2μm thin film of bis (2-ethylhexyl)sebecate, and ITO with a 100μm polyimide layer covered with two different liquid crystals ZLI-3417 and E7. Both glass and ITO coated glass were cleaned by sonication in acetone, isopropanol, then with nanopure water. In the case of the bis (2-ethylhexyl)sebecate on ITO coated glass, the bis (2-ethylhexyl)sebecate is then spun on to the ITO coated glass at spin parameters of 500 rpm for 5 seconds then 3000 rpm for 30-120 seconds to produce various thicknesses. The thickness of the most common spin parameters of 500 rpm for 5 seconds then 3000 rpm for 60 seconds was found using interferometric measurements. A representative spectrum that the thickness of the bis (2-ethylhexyl)sebecate layer was calculated from is shown in figure 2.14.

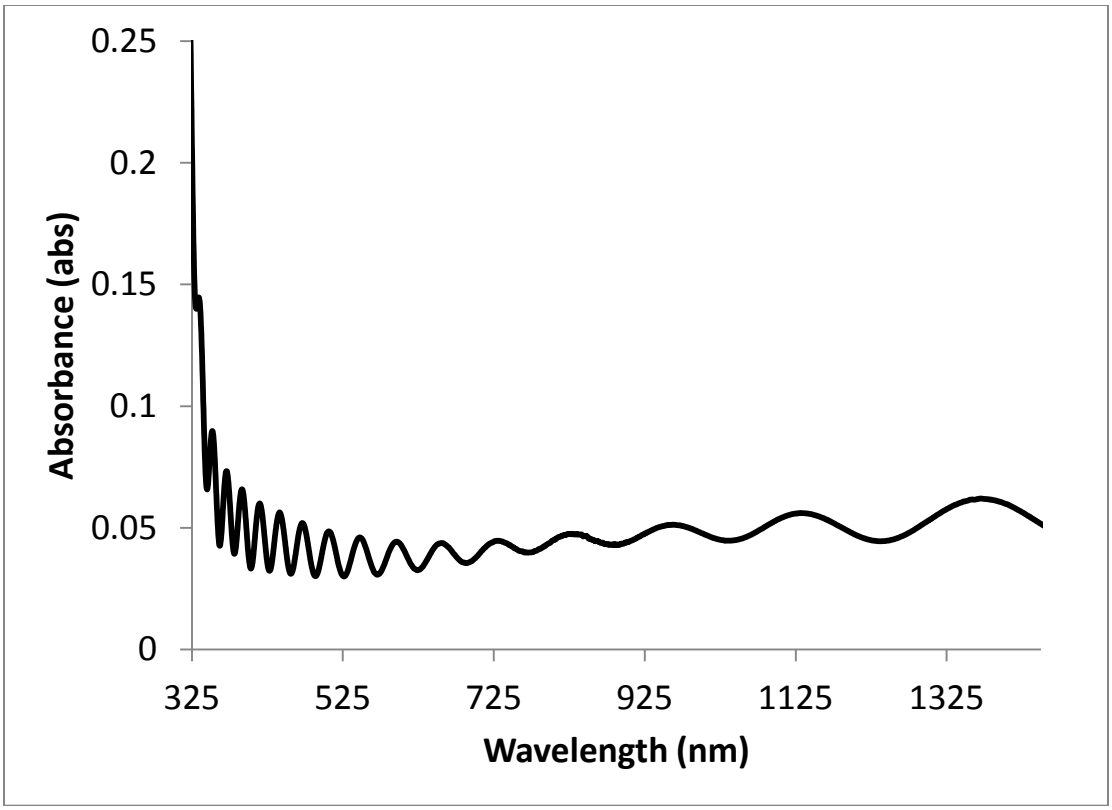

Figure 2.14
Interferometric UV-Vis spectrum of bis (2-ethylhexyl) on ITO coated glass sebecate used to calculate thickness of thin film

Three slides were spun at the same parameters and UV-Vis spectra were taken of each slide with a JASCO D-670 spectrophotometer. In the case of a thin film on the surface of another material both of the interfaces between the thin film and the film and the air reflect light. The constructive and destructive interference of the reflection from these two surfaces depends upon the optical path lengths of the two reflections. The interference pattern shown in figure 2.14 can be used to determine the thickness of the film by using the equation[4]

$$d = \frac{m}{2D_n \sqrt{n^2 - \sin^2\theta}}$$

Where:

d = film thickness

m =number of fringes in region used

θ =angle of incidence

D_n =size of region used

JASCO spectra manager software was used with a refractive index of 1.45 and a range of 342.5-1430nm to calculate the thicknesses shown in table 2.1.

Table 2.1 Bis (2-ethylhexyl)sebecate thin film thicknesses

	Thickness (μm)
slide 1	1.624
slide 2	1.751
slide 3	2.181
average	1.852
standard deviation	0.291913

In the case of the polyimide coated ITO glass a polyimide mixture is spun on to the ITO glass slide at parameters of 4000 rpm for 30 sec to form an approximately 100 μm thick layer. The polyimide coated ITO glass slide is then heated to 130 °C and held for 15 minutes then heated at 5 °C per minute to 250 °C and held for 30 minutes to cure the polyimide. After curing, the polyimide slide is rubbed with optical cleaning paper unidirectionally to establish the in-plane orientation of the liquid crystal.

2.4 Determining Extinction Coefficient

To determine the extinction coefficient of tetracene in hexanes a series of solutions of varying concentration was made. UV-Vis spectra were then taken of the resulting solutions, a representative spectrum is shown in figure 2.15.

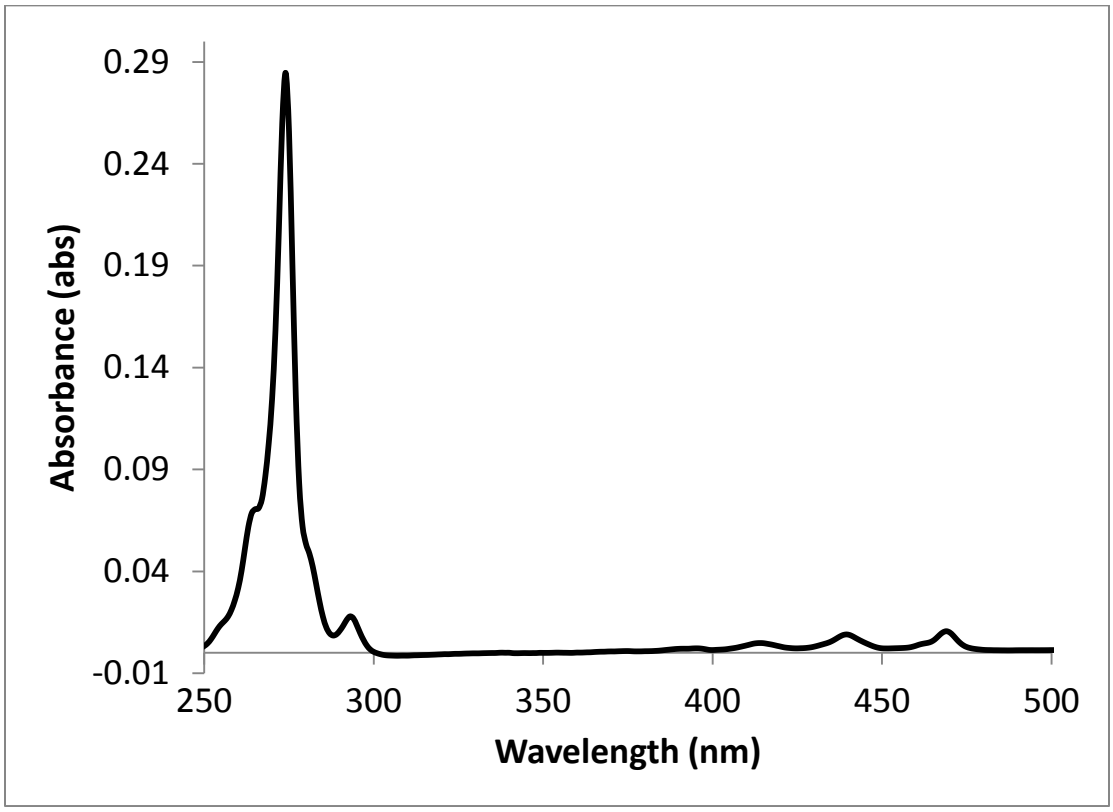

Figure 2.15
Representative UV-Vis spectra of tetracene in hexanes note the peak in the visible at 470 nm corresponding to the ^1L_a band and the peak in the UV region at 274 nm corresponding to the ^1B_b which will use to quantify concentration of solutions because of its large extinction coefficient

The baseline correction method used for all UV-Vis measurements involved subtracting the absorbance at 350nm from the entire spectrum. The extinction coefficient was determined to be 320,000 M^{-1} in hexanes, which is slightly higher

than the reported literature value[5] of 270,000 M^{-1} in pentane. The calibration curve shown in figure 2.16.

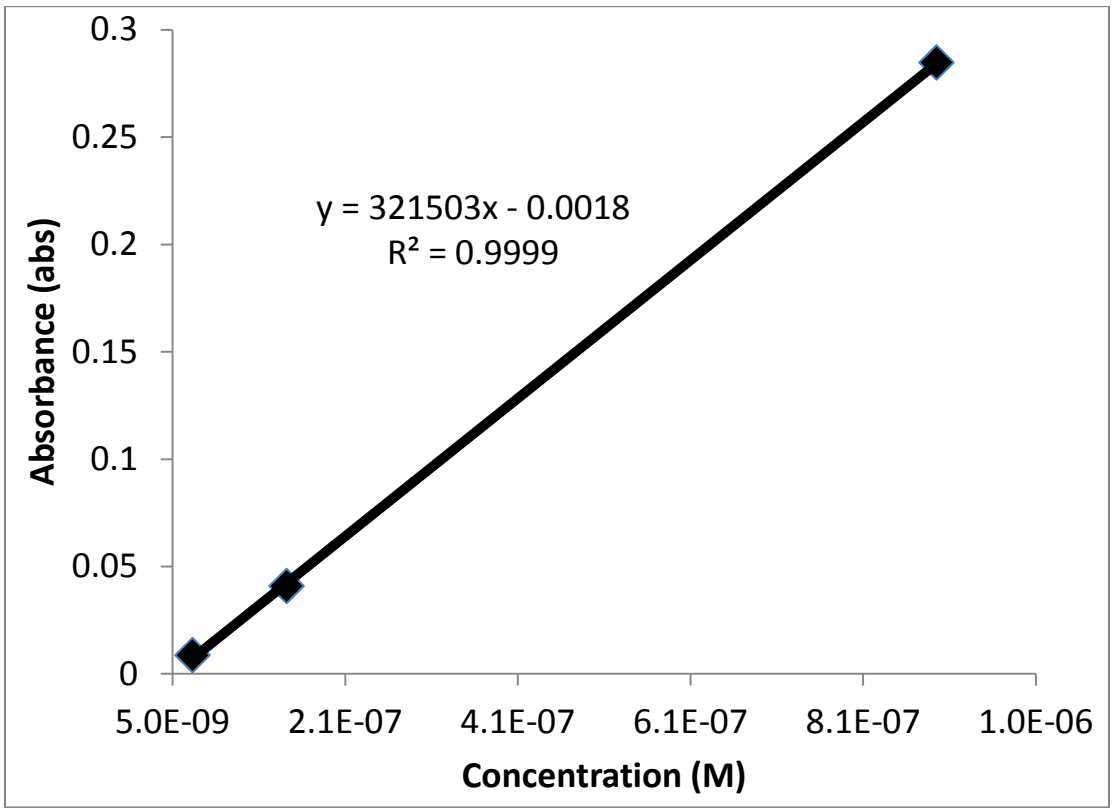

Figure 2.16
Plot of peak absorbance at λ=274 nm used to calculate a extinction coefficient of ~320000L mol^{-1} cm^{-1}

[1] F. Scott Wilkinson, Ronald F. Norwood, Joseph M. McLellan, L. Rhys Lawson, and David L. Patrick **J. AM. CHEM. SOC. 2006**, 128, 16468-16469

[2] Kevin Bufkin, MS thesis, Western Washington University, Bellingham, WA, 2010

[3] R. J. Kee, M. E. Coltrin, P. Glaborg, "Chemically Reacting Flow Theory and Practice", John Wiley and Sons, Hoboken, N.J. (2003).

[4] Andrew R. Hind, Lisette Chomette, Varian UV at work, No. 90, 1-5

[5] Benoy B. Bhowmik, Tapan K. Paul, "Charge-transfer interaction of carbontetrachloride with tetracene", spec. Acta. **1982,** 38A, 6, 713-715

CHAPTER 3

3.0 **Introduction**

In this chapter film growth will be discussed in detail, starting with a qualitative description of the deposition and growth process of crystals on a surface. The author will also discuss the effect of crystal growth in various liquid thin films and compare the method presented in this thesis to other similar methods. Additionally a model for gas phase aggregation and hydrodynamic deposition will be presented as well as a discussion on crystal growth kinetics.

3.1 **The Growth Process**

As described in greater detail in chapter 2, tetracene is placed in an aluminum crucible, heated to its sublimation point, the sublimate is carried by argon gas and the gas carrying the tetracene impinges upon the substrate creating an axisymmetric stagnation point at the substrate. Tetracene molecules diffuse across the static boundary layer and land on the surface of the substrate which has a thin liquid layer, deposited via spin coating on its surface. As tetracene molecules are deposited they dissolve in the liquid layer. This continues until the liquid layer becomes saturated, saturation can take less than a minute to several hours depending upon the liquid thickness, its saturation concentration, and the flux rate. At a certain critical concentration above the saturation concentration crystals begin to nucleate. Figure 3.1A shows a sample at this stage of growth, when new crystals are in the process of

forming. The image was taken using polarized optical microscopy of a sample in the deposition chamber as film growth was occurring. For this sample saturation of the liquid layer of bis(2-ethylhexyl)sebecate was achieved in less than 5.3 minutes. The first crystals to nucleate are fairly well dispersed and small. As deposition proceeds new crystals nucleate and previously nucleated crystals grow until the crystals have grown/nucleated so close together that further nucleation essentially ceases. This stage of growth, the steady-state regime, is shown in figures 3.1B and C. After approximately 10 minutes existing crystals begin incorporating dissolved tetracene at the same rate that new tetracene is being introduced to the system. As a result of the nucleated crystals being so densely distributed newly dissolved tetracene is unlikely to find enough material to nucleate a new crystal before it is incorporated into an already formed crystal. During the steady-state regime crystals gradually grow in size until they coalesce. Note the large increase in crystal nucleation density when comparing frames A and B in figure 3.1. This stage is when crystals are first starting to nucleate and in contrast there is very little change in density when comparing frames B to C in figure 3.1.

The composition of the thin liquid is an important parameter to optimize. The semiconductor (in this case tetracene) has to be soluble enough in the liquid to dissolve but not so soluble that it takes a great deal of material to reach the saturation point. To explore this parameter several different liquids were investigated.

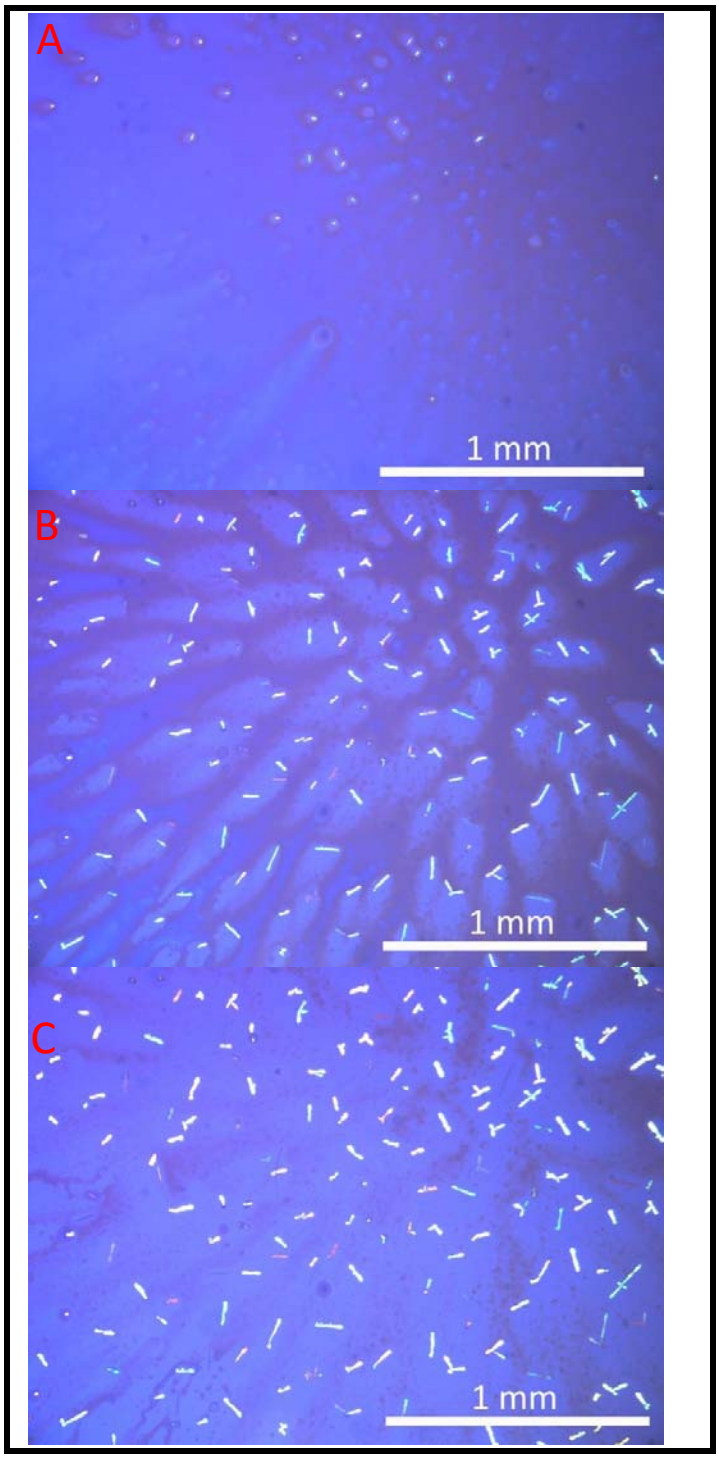

Figure 3.1
Tetracene thin film growing in bis (2-ethylhexyl)sebecate. Images taken *in situ* at different times during deposition with a long working distance cross polarized optical microscope A) 5.3 minutes B) 10.3 minutes C) 20.3 minutes of deposition

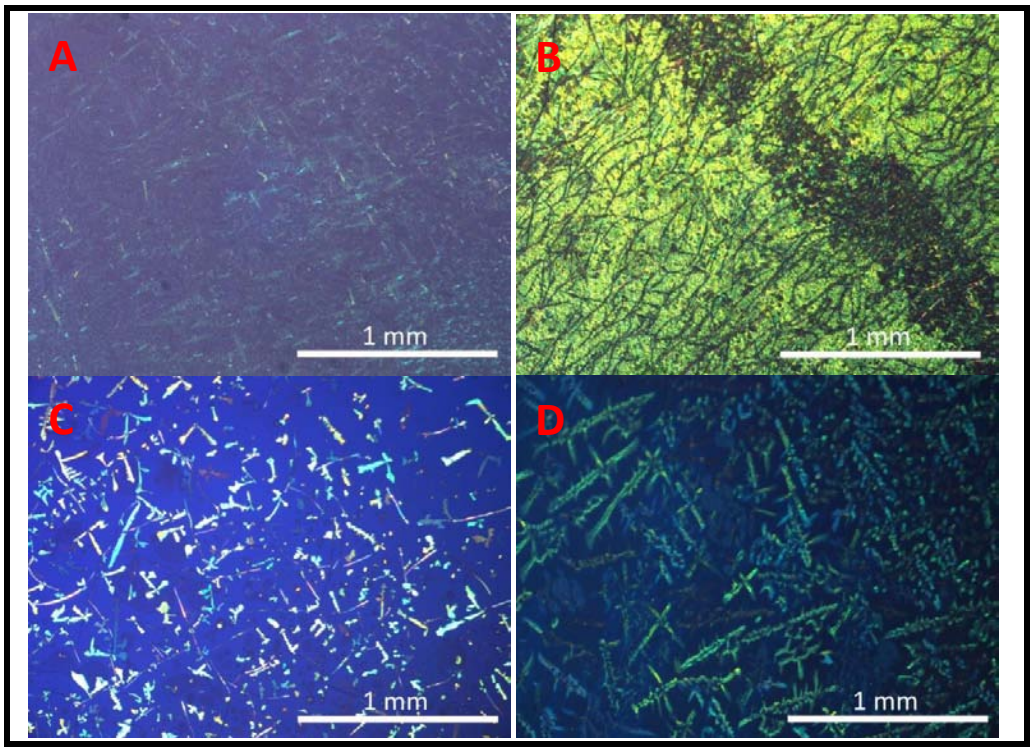

Figure 3.2
Images taken with cross polarized optical microscopy of tetracene films grown in different liquid thin films A) 2,2'-thiodiethanol B) liquid crystal E7 C) bis(2-ethylhexyl)sebecate D) liquid crystal ZLI 3417

A selection of films grown with different liquid layers, two liquid crystals (E7 & ZLI 3417) and two isotropic liquids (2,2‟-thidiethanol and bis (2-ethylhexyl)sebecate), are shown in figure 3.2. Note that both 2,2‟-thidiethanol and E7 produced poor films with very small crystals and a very high nucleation density while bis (2-ethylhexyl)sebecate and ZLI 3417 produced larger crystals with lower nucleation density. Also note in figure 3.4D that the light passing through all the crystals is of a similar brightness, this qualitatively indicates a degree of macroscopic order between crystals. Thus most promising is ZLI 3417, not only did ZLI 3417 produce large crystals, but the crystals show a degree of alignment.

In contrast to growth in a liquid layer, as discussed above, dry based growth, growth with no liquid layer produces crystals an order of magnitude smaller than the crystals grown in a liquid layer. Scanning electron microscopy (SEM) images of a tetracene thin film grown on ITO coated glass are shown in figure 3.3. Note the very small size of the crystallites, as well as the persistent problem of more than one form of crystal. As discussed in chapter 1, if this film were to be made into a device it would have very poor performance because of its small crystal size creating many energy barriers to retard the motion of charge carriers. The small size of the crystallites is evidence of an important deposition parameter, the ratio of flux to diffusion rate: if the flux is high and the diffusion length is short material cannot travel far before encountering either a nucleated crystal or enough monomers to nucleate a new crystal.

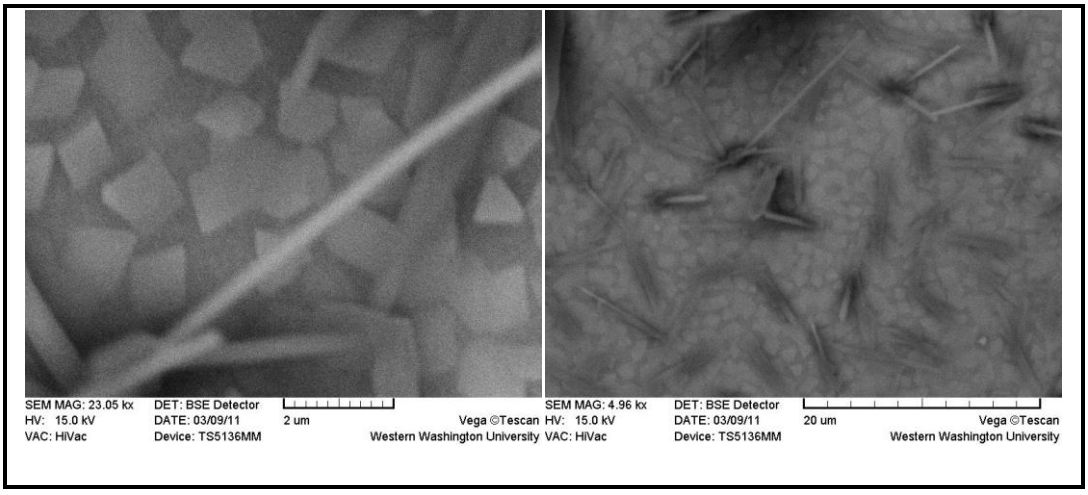

Figure 3.3
Two SEM images of a thin film of tetracene grown on ITO coated glass showing two general crystal shapes and crystallite sizes of <10µm

The relationship between deposition rate and nucleation density is readily observed in figure 3.4. Both 3.4A and B are tetracene thin films grown in an approximately 2µm

thick layer of bis(2-ethylhexyl)sebecate. 3.4A had a deposition rate of 6.523×10^{-6} mol m^{-2} min^{-1} while that shown in 3.4B had a rate between 1.6×10^{-7} mol m^{-2} min^{-1} and 3.7×10^{-6} mol m^{-2} min^{-1}. The increased deposition rate of the former leads to the greater nucleation density observed.

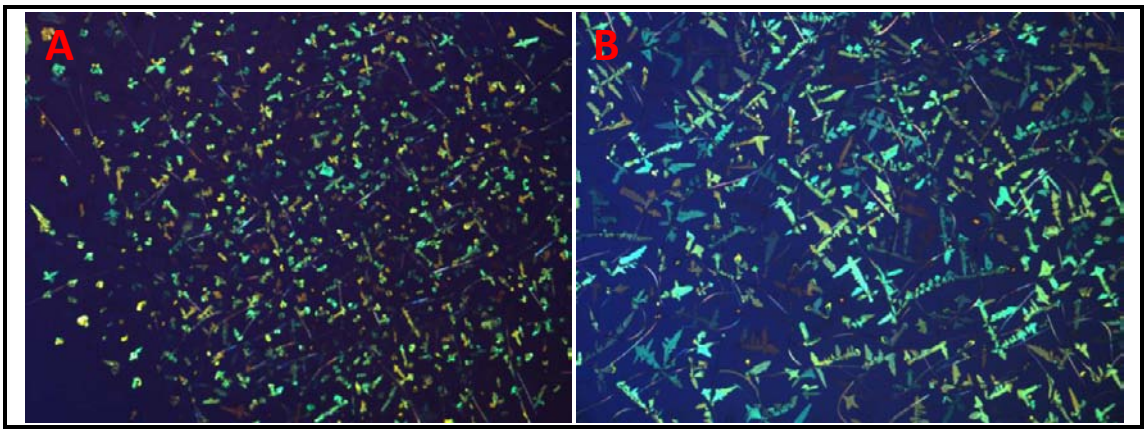

Figure 3.4
A) Cross polarized optical microscopy image of tetracene thin film grown in bis(2-ethylhexyl)sebecate at a deposition rate of 6.523×10^{-6} mol m^{-2} min. B) Cross polarized optical microscopy image of tetracene thin film grown in bis(2-ethylhexyl)sebecate at a deposition rate between 1.6×10^{-7} mol m^{-2} min^{-1} and 3.7×10^{-6} mol $m^{-2}min^{-1}$.

3.2 Film Characterization

Shown in figure 3.5A is a UV-Vis spectrum of a thin film of tetracene grown on ITO coated glass. Note the red shift of the peaks and the Davydov splitting around 525 nm arising from electronic interaction of neighboring tetracene molecules indicating the film is somewhat crystalline in contrast to the spectrum taken of tetracene in a solution of hexanes shown in figure 3.5B where tetracene molecules are isolated from one another by the solvating hexane molecules.

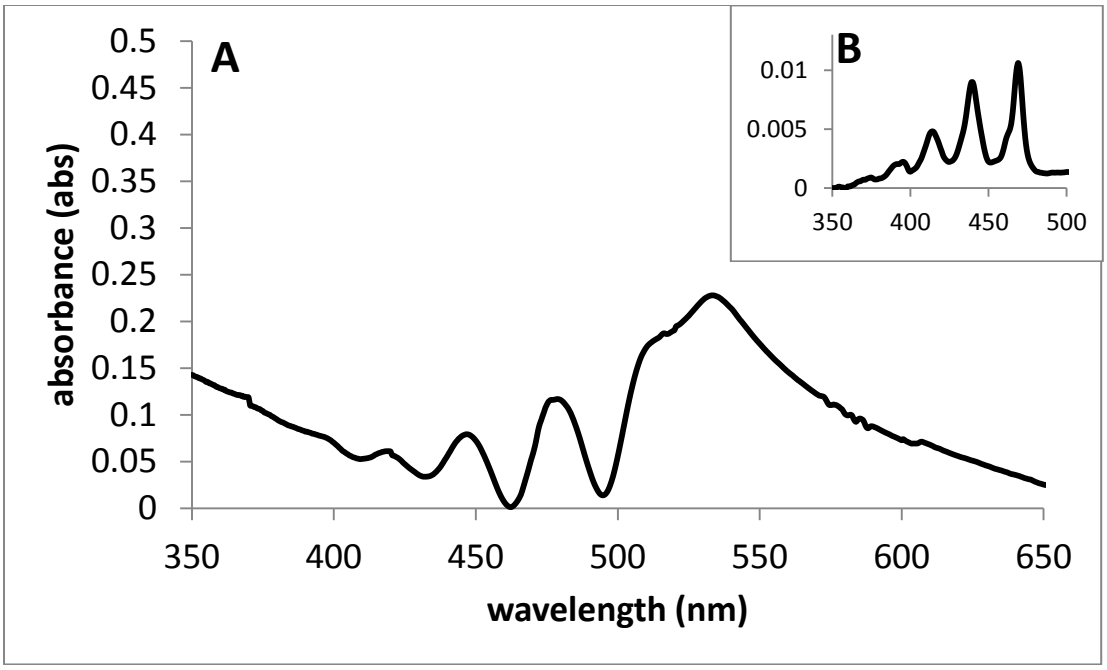

Figure 3.5
A)UV-Vis spectrum of tetracene thin film grown on ITO coated glass exhibiting Davydov splitting of the peak at 529 nm and the red shift compared to B)the spectrum taken in hexanes.

Figure 3.6 shows an image taken by atomic force microscopy (AFM) of a tetracene crystal grown in bis(2-ethylhexyl)sebecate during the steady-state stage. Note that there are no smaller crystals apparent in the AFM image which leads one to the conclusion that large optically visible crystals are the only crystals present at this stage of growth. Several images of different crystals from the same sample were taken by AFM and the average height vs. crystal area is plotted shown in figure 3.7. Note that the 2D area the crystal occupies seems to have no correlation with the thickness of the crystal. It is important to note that this lack of correlation of thickness to 2D area was only from one sample with one deposition time and rate. Further experiments such as finding the average thickness of crystals at varying total coverage e.g., when crystals are still nucleating or when coalescence is just beginning

are necessary to fully understand the dependence of crystal thickness upon 2D area of crystals.

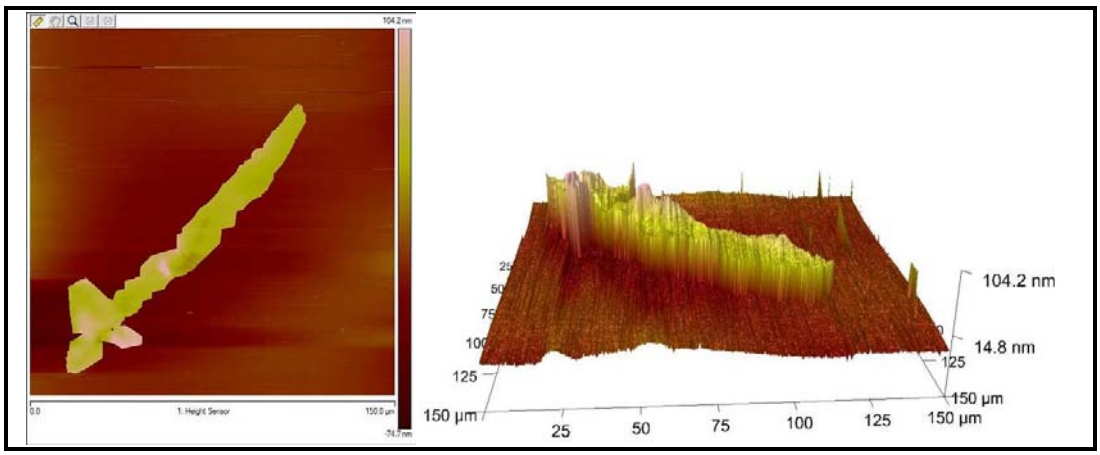

Figure 3.6
AFM image of tetracene crystal grown in bis(2-ethylhexyl)sebecate on ITO coated glass

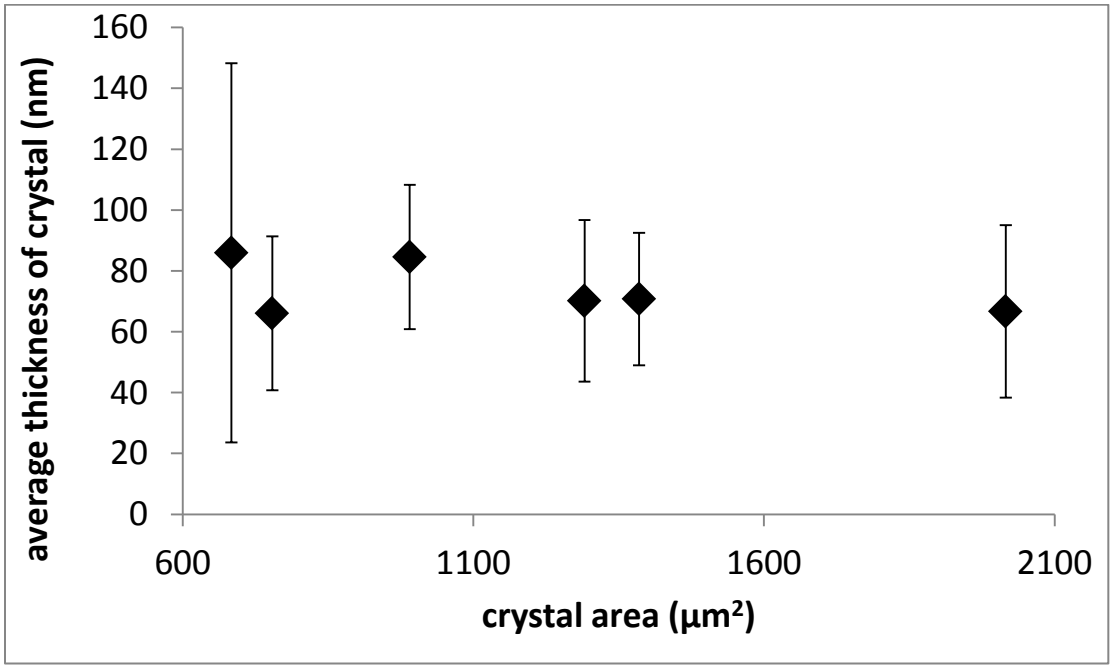

Figure 3.7
2D area occupied by crystal vs. average thickness of that crystal, determined via AFM. Note the similar thickness of crystals with vastly different 2D areas.

To illustrate that the deposited crystals are tetracene and show highly crystalline behavior an x-ray diffractogram was taken, shown in figure 3.8 is a diffractogram of a thin film of tetracene grown in bis(2-ethylhexyl)sebecate. Peaks at 7.21°, 14.47°, 21.83°, 29.25°, 36.85°, and 44.45° agree with the literature[1] corresponding to the Bragg indices (001), (002), (003), (004), (005), and (006) for tetracene.

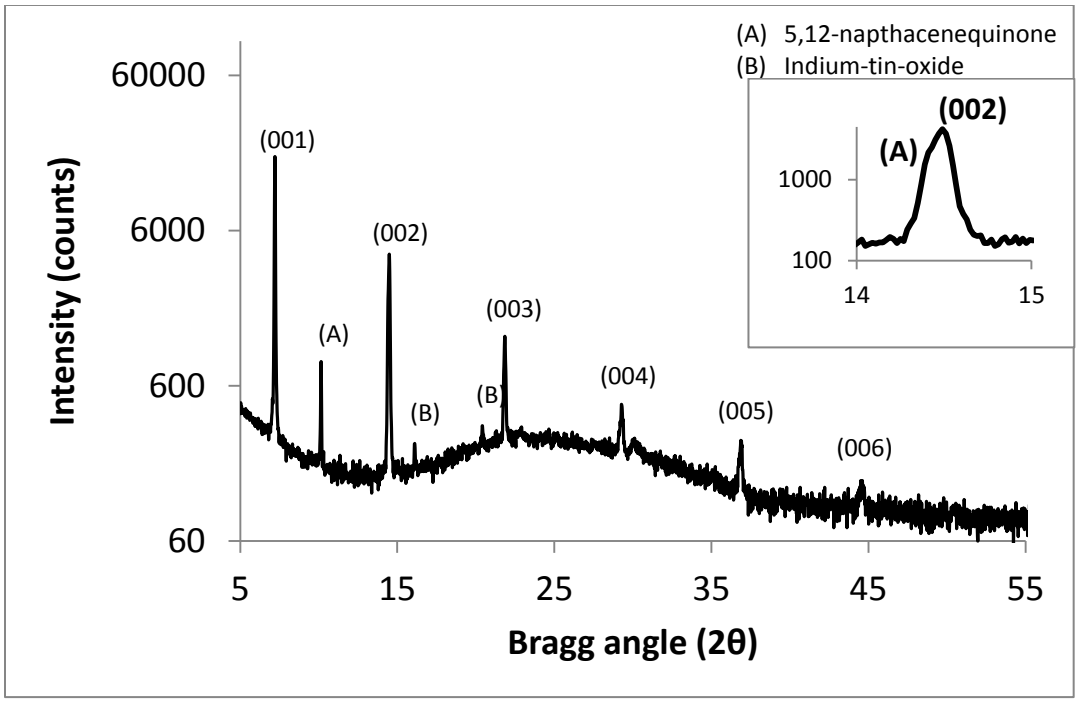

Figure 3.8
Diffractogram of tetracene thin film grown in ~2µm bis(2-ethylhexyl)sebecate layer. Sample had a run time >1000 minutes and a high coverage. An expansion of the (002) peak of tetracene can be seen in the inset. The 5,12-napthacenequinone shoulder on the tetracene (002) peak is readily apparent in this expansion.

A peak at 10° was confirmed to be the main impurity 5,12-napthacenequinone via a x-ray diffractogram of a reference sample of 5,12-napthacenequinone, shown in figure 3.9. Note the major peak at 10° that also present on thin films of tetracene grown in bis(2-ethylhexyl)sebecate. The 5,12-napthacenequinone peak at

approximately 14° is evident as a shoulder on the (002) peak of tetracene in the inset of figure 3.8. Peaks at 16.1° and 20.3° line up with peaks from the literature that are associated with ITO.[1]

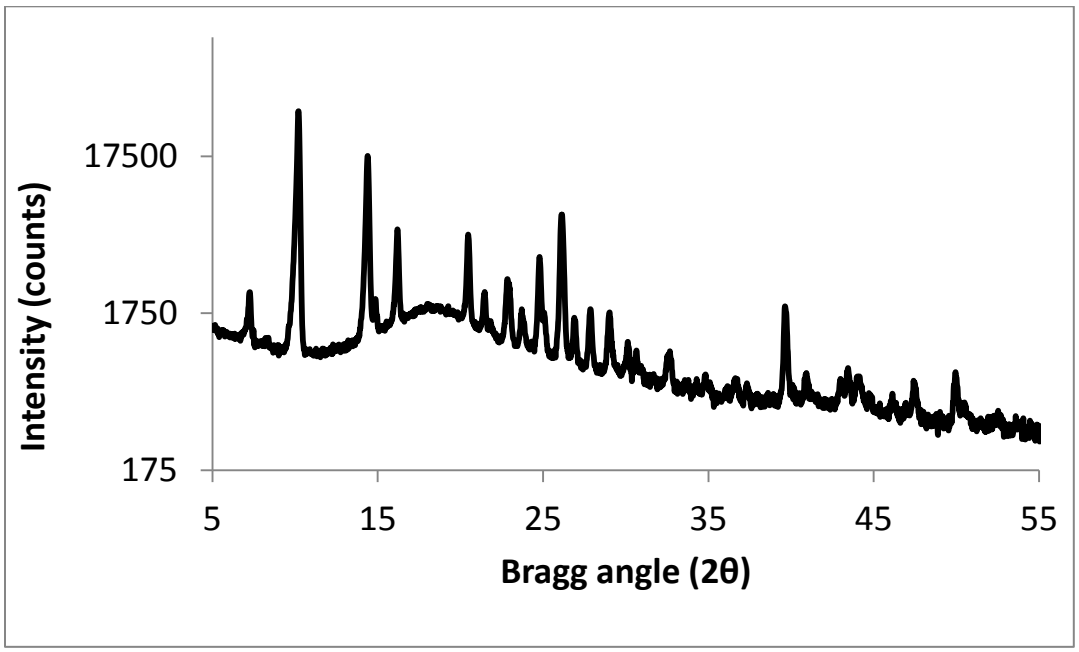

Figure 3.9
Diffractogram of 5,12-napthacenequinone taken as a reference from a powder sample. The two highest intensity peaks at ~10° and ~14.5° these were the two peaks used to identify the impurity in the tetracene films

The multiple well formed peaks show that films grown in bis(2-ethylhexyl)sebecate are highly crystalline. In contrast an x-ray diffractogram of dry based growth of tetracene on ITO coated glass is shown in figure 3.10 and shows a much less crystalline film. Note the persistence of the impurity peak at 10°.

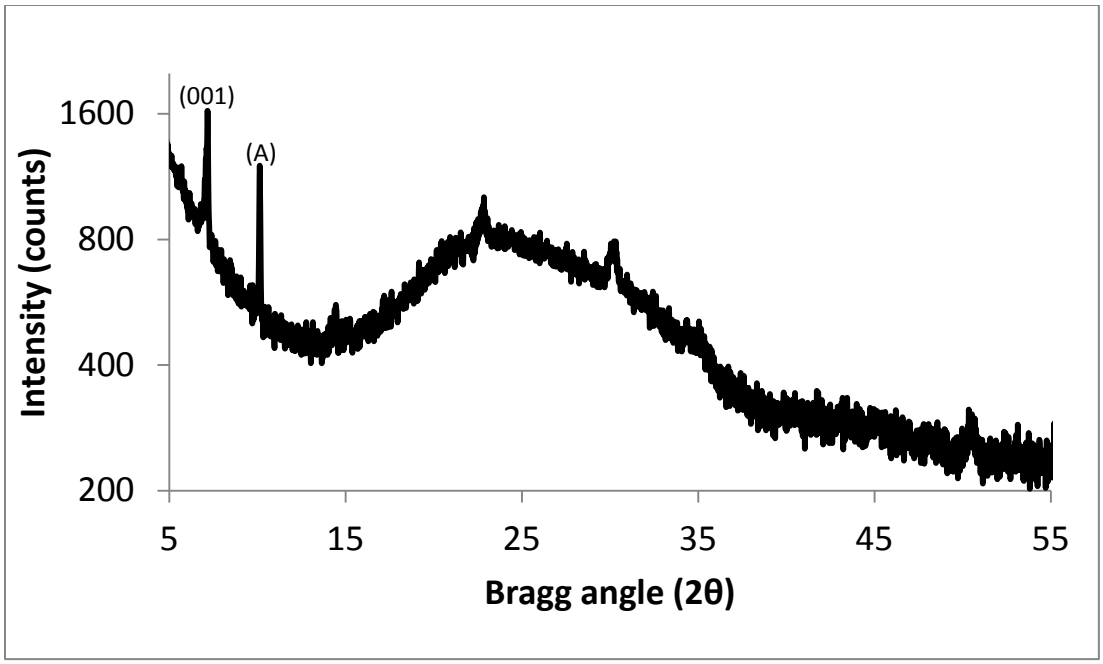

Figure 3.10
Diffractogram of tetracene thin film grown on ITO coated glass, showing the peak (A) at 10° associated with 5,12-napthacenequinone and the (001) peak associated with tetracene at 7.2°

3.3 **Impurity Characterization**

One source of concern has been the presence of more than one type of crystal. The crystal type that is more advantageous for the growth of high quality of organic semiconductor thin films is planar and grows as or into compact shapes like shown in figure 3.11A. The other type of crystal that has persistently shown up in deposition is more needle or wire like and is shown in figure 3.11B

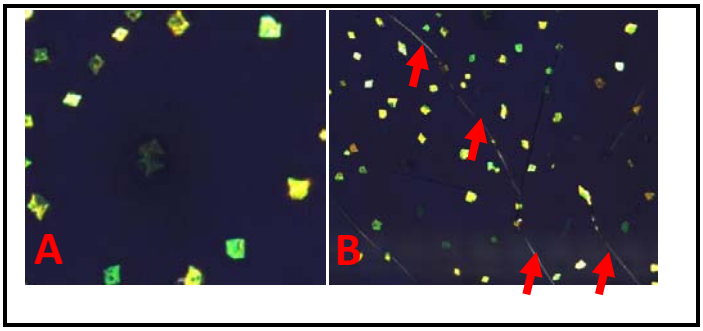

Figure 3.11
Images of tetracene grown in bis(2-ethylhexyl)sebecate. Insert A) shows the desired compact shapes of nucleate crystals while insert B) shows the presence and character of the needle impurities highlighted with arrows.

These needle crystals cause problems when determining crystal density during analysis of the growth of thin films. Crystal density is a useful tool for analyzing this growth and is defined as the number of crystals per unit area. Crystal density is determined by observing the number of discrete crystals in a given frame. If two crystals coalesce, even with differing crystal lattices they are observed to be a single crystal. This assumption works when the crystals are compact but if a needle crystal grows through multiple compact crystals all of those crystals are now erroneously assumed to be one crystal when measuring crystal density. Additionally, if these needle-like crystals are made of the same material as the more advantageous crystal type, they are taking up material that would have been used to expand existing compact crystals.

The following observations suggest that the needles are formed of an impurity rather than tetracene. First, there is no other crystal morphology of tetracene reported in the literature. Secondly, the needles do not appear until after the nucleation of the compact shaped crystals. Thirdly, the needle shaped crystals seem to appear even

when utilizing different liquid layers or no liquid layer at all. All of these facts point towards the idea that these needle shaped crystals are not a different polymorph of tetracene and rather an impurity. Images of needle crystals grown in multiple solvents are shown if figure 3.12.

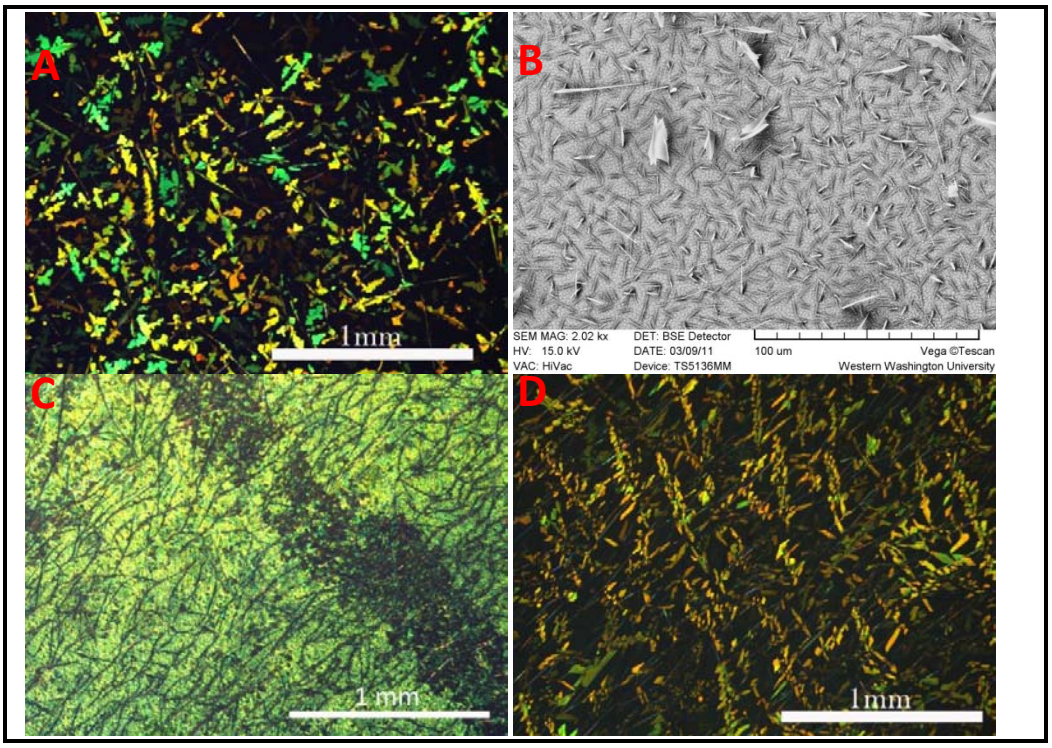

Figure 3.12
A) tetracene grown in bis(2-ethylhexyl)sebecate B) SEM image of tetracene grown on ITO coated glass C) tetracene grown in 2,2'-thiodiethanol D) tetracene grown in ZLI 3417. Images A, C, and D captured by cross polarized optical microscopy. Note the presence of needle like crystals in all images.

As previously shown by XRD (in figures 3.8 and 3.9) 5,12-napthacenequinone is the major impurity in both the dry based film growth and film growth in bis(2-ethylhexyl)sebecate. This can also be seen in the FTIR spectrum shown in figure 3.13 with the presence of a peak at 1675 cm^{-1} in an infrared spectrum, using K.

Bufkin"s calibration curve[2] the tetracene thin film is approximately 23% 5,12-napthacenequinone.

23% is an extremely high concentration for an impurity several factors may have contributed to an increase in impurity concentration. First, the argon flowed through the apparatus was not UHP and it was not run through an oxygen scrubber before entering the apparatus. Second, the apparatus itself may not have been perfectly leak free. Third, a more extensive purging could have been performed before deposition but this would have added a prohibitively long amount of time to each deposition and was deemed unnecessary by the author at that time. If oxygen was introduced by a minute leak or via the argon into the apparatus during deposition the tetracene vapor may have oxidized into 5,12-napthacenequinone. Further, the samples used to

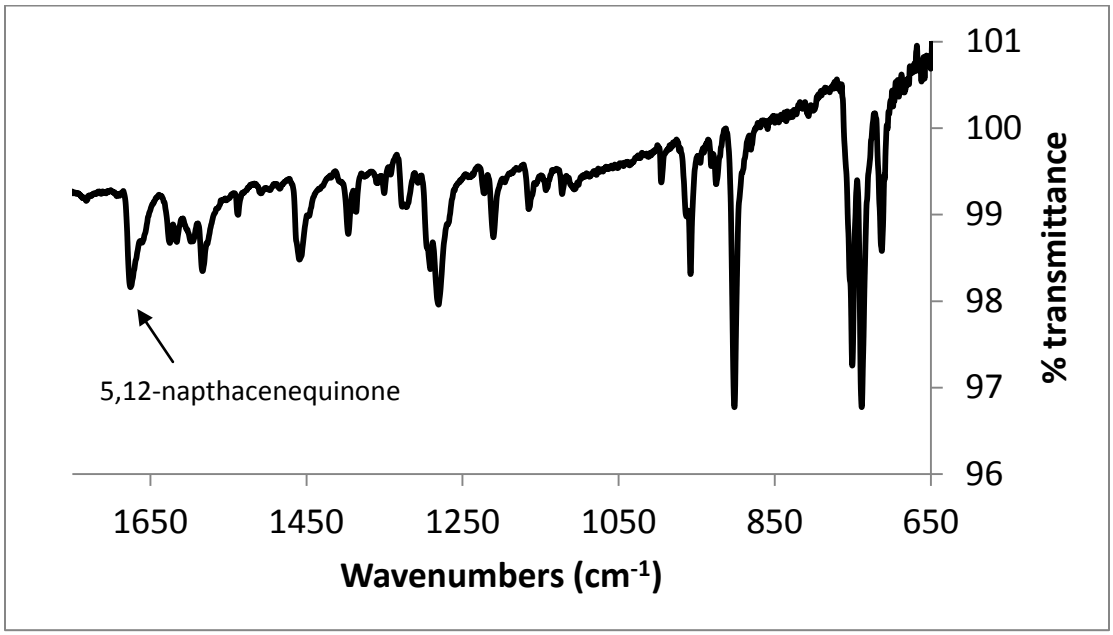

Figure 3.13
FT-IR spectrum of tetracene thin film grown in bis(2-ethylhexyl)sebecate highlighting the 5,12-napthacenequinone peak at 1675cm^{-1}.

determine 5,12-napthacenequinone concentration were allowed to sit on the bench top for several weeks before being probed overnight by XRD and imaged by SEM. These factors may have contributed to an especially high concentration of impurity in the samples used to determine impurity concentration.

3.4 Gas Phase Aggregation and the Hydrodynamics of Deposition.

[Portions of this section are based on a manuscript in preparation by Shaw, D., Bufkin, K., Lund, C., Baranov, A., and Patrick D.L.]

After the gas flow exits the nozzle it behaves like a semi-confined jet. Numerous studies have examined the behavior of confined and free jets, which occur in a wide range of contexts, from rockets[3] to flames,[4] volcanoes,[5] and effluent discharges at factories and power plants.[6,7] Qualitatively, it is found that for moderately large Reynolds numbers, but below the onset of instability (~100 < Re < ~2000), a circular jet injected into a stagnant fluid of the same density develops into a steady slender flow. As the jet entrains fluid from the surroundings it gradually expands and the centerline velocity decreases. For very large distances the flow eventually becomes unsteady.[8,9] Figure 3.14 illustrates free jet behavior for a range of different Reynolds numbers. The conditions used in our experiments were typically between the first and second panels, with $50 < Re < 500$. It can be seen that the jet remains laminar for many times its initial diameter, and that the angular rate of spreading is very small.

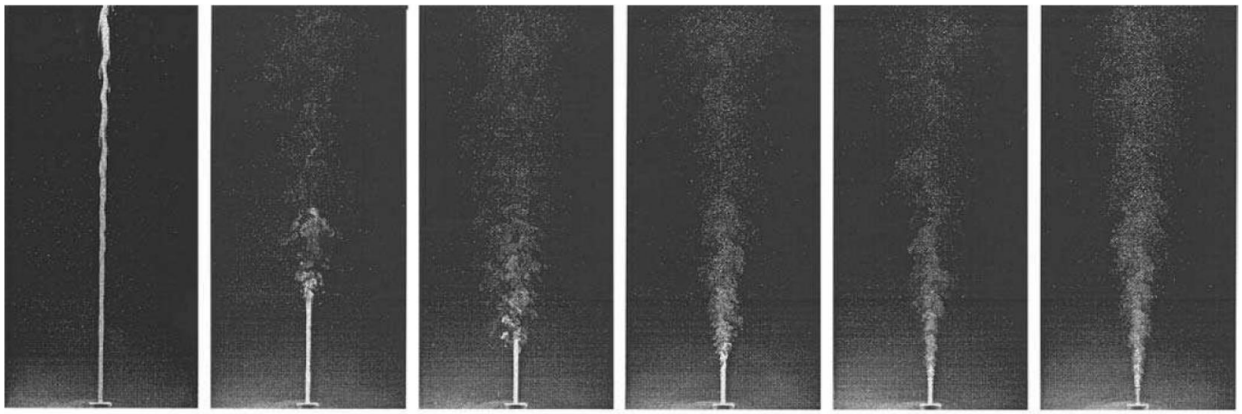

Figure 3.14 Instantaneous images of the evolution of a round non-buoyant jet with increasing Reynolds number. From Ref. [10].

Depending on the velocity profile at the nozzle exit (flat or Poiseuille profile), the hydrodynamics in the near-field region of jet establishment ($z < \sim 10a$) can differ significantly from the situation farther downstream. The confining effects of the substrate and shape of the nozzle exterior also affect the flow. Due to the large aspect ratio of the needle ($L/a = 13$), the initial velocity profile of the jet can be expected to be approximately parabolic (Poiseuille profile), diffusing toward a flat profile as it travels to the substrate. To produce a relatively flat profile while retaining laminar flow, and also to minimize confinement effects resulting from the exterior shape of the needle, a blunt needle was used separated from the substrate by a scaled distance $z^*/a \approx 8$. However these steps are probably insufficient to entirely eliminate the aforementioned complexities, and there are further complicating effects resulting from confinement and circulating gases within the deposition chamber, so we do not attempt here to make an accurate treatment of the full hydrodynamics. Instead we adopt a very simple model, assuming a flat velocity profile over a circular area equal

to the size of the nozzle opening with laminar flow normal to substrate, Similar to the image shown in figure 3.15.

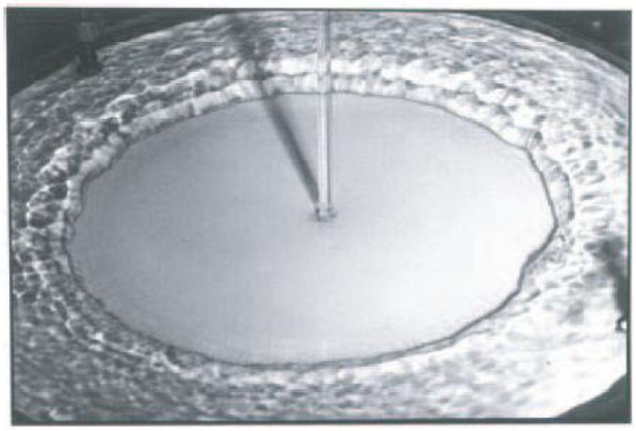

Figure 3.15
From: "Heat transfer by impingement of circular free-surface liquid jets", Lienhard V, J. H., 18th National & 7th ISHMT-ASME Heat and Mass Transfer Conference, Jan 4 – 6, 2006, Guwahati, India.

The impinging jet can be modeled as three-dimensional axisymmetric stagnation point flow, a classical problem in fluid mechanics.[11] Because the liquid layer coating the substrate was very thin, we treat the flow as impinging on a flat, incompressible surface (experiments showed that the deposition rates on dry and liquid-coated surfaces did not differ substantially, indicating the presence of the liquid did not affect mass transport). Along the z-direction the flow field can be divided into two regions: (i) a stagnation boundary layer immediately adjacent to the substrate, and (ii) an outer flow region. In the outer flow region the streamlines are hyperbolic with the velocity components of the gas approximately given by:[12]

$$v_r = \alpha r \qquad (1a)$$

$$v_z = -2\alpha z \tag{1b}$$

where α is a constant and r is the radial distance from the center of the impinging jet. Near the substrate a static boundary layer develops due to the no-slip condition at the surface. For uniform laminar flow, near the center of the impinging jet (that is, for $r \leq \sim a$) the thickness of the boundary layer ε is nearly constant and is given by[13]

$$\varepsilon \approx \frac{z^*}{Re^{1/2}} \frac{0.2365}{Re^{1/2}} + 1.892 + \frac{0.0559}{Re}^{1/2} \approx 1.375 z^* Re^{-1/2} \tag{2}$$

where the Reynolds number $Re = z^* U \rho_g / \mu$, z^* is the distance between the nozzle and substrate, U is the jet velocity far from the substrate, μ is the gas dynamic viscosity and ρ_g is the gas density. Since the typical Reynolds numbers used in the experiment were in the range 50 ~ 500, well below the onset of turbulence, the flow conditions are assumed to be laminar.

Note from Eq. 1b that the vertical component of the gas velocity is independent of radial position, and hence the amount of time required for a fluid parcel exiting the nozzle to reach a given height z depends only on z, and not on its radial position. Therefore in a system where gas-phase particles undergo continuous growth through aggregation, there is no radial variation in particle size. Also note that according to equation 2 the thickness of the boundary layer is uniform near the stagnation point,

and hence the deposition rate in the region directly above the nozzle should also be nearly uniform. These properties of axisymmetric stagnation-point flow make it particularly suitable for depositing highly uniform films.

The flux of particles reaching the surface under conditions of axisymmetric stagnation point flow has been treated by several groups. Forrest and coworkers[14] calculated the diffusive flux of particles across the boundary layer by assuming the substrate acts as a perfect sink (unity sticking coefficient) and applying conservation of mass to arrive at:

$$J = c_o \frac{U}{1 + U\varepsilon/D} \tag{3}$$

where J (m^{-2} s^{-1}) is the flux to the substrate, c_o is the particle concentration at a distance ε from the substrate, U is the jet velocity far from the substrate, and D is the particle diffusion coefficient. However these authors used an incorrect expression for the boundary layer thickness, which can lead to a considerable error in the calculation of the flux rate near the stagnation point.

Earlier, Chin and Tsang[15] proposed an asymptotic solution for the flux expanded in terms of the Schmidt number, $Sc = \mu/\rho_g D$:

$$J = 0.85002 c_o D \sqrt{\frac{\pi U}{8R}} Sc^{\frac{1}{3}} g(Sc) \quad (4)$$

where $Sc = 1 - \frac{0.084593}{Sc^{1/3}} - \frac{0.016368}{Sc^{2/3}} - \frac{0.0057398}{Sc} + \frac{0.0014288}{Sc^{4/3}} + \frac{0.0013088}{Sc^{5/3}} + \cdots$ and R is the radius of the substrate.

Here we follow the treatment of Cooper and coworkers, who expressed the particle flux rate in terms of the Sherwood number:[16]

$$J = c_o Sh \frac{D}{2r_p} \quad (5)$$

where r_p is the particle radius, and Sh is the Sherwood number, defined as the dimensionless concentration gradient at the substrate:

$$Sh \approx \frac{0.7761 r_p}{D^{1/3}} \left(\frac{U}{z^*}\right)^{1/2} \left(\frac{\rho_g}{\mu}\right)^{1/6} \quad (6)$$

All three approaches predict $J \sim U^{1/2}$ for monodisperse particles, and flux rates that agree to within 50% of each other. Note that inertial effects are not significant for the very small particles considered here, i.e. those with Stokes numbers $St = Um_i / 12\pi\mu r_i < \sim 0.1$.[17]

If no aggregation occurs among gas phase molecules in transit to the liquid layer, then D is just the diffusion coefficient of a monomer, and $J \sim U^{\beta}$, where $\beta = 1/2$. This was the situation in the experimental system employed in Ref. 18, where a high temperature gas flow was used to prevent gas-phase aggregation and the predicted value $\beta = 1/2$ was confirmed. However at lower gas temperatures such as those used the present work, some coalescence of monomers can be expected to occur, resulting in a time-dependent distribution of aggregate sizes whose diffusion coefficients D_i depend on the number of monomers i in the aggregate. The effect of this is illustrated in figure 3.16, which plots the deposition efficiency, J/c_o, defined as the fraction of particles incident on the static boundary which reach the liquid, against particle size. As can be seen, mass transport across the boundary layer strongly favors small particles. To provide some context for this result, the estimated size of the critical nucleus for tetracene in bis(2-ethylhexyl)sebecate (please refer to Section 3.6) is also shown in the figure 3.16. The deposition efficiency of particles the size of the critical nucleus is over 100 times smaller than it is for monomers. This may help explain why, even though some aggregation occurs in the gas phase, very few particles large enough to serve as nuclei for new crystals actually reach the liquid layer (see below).

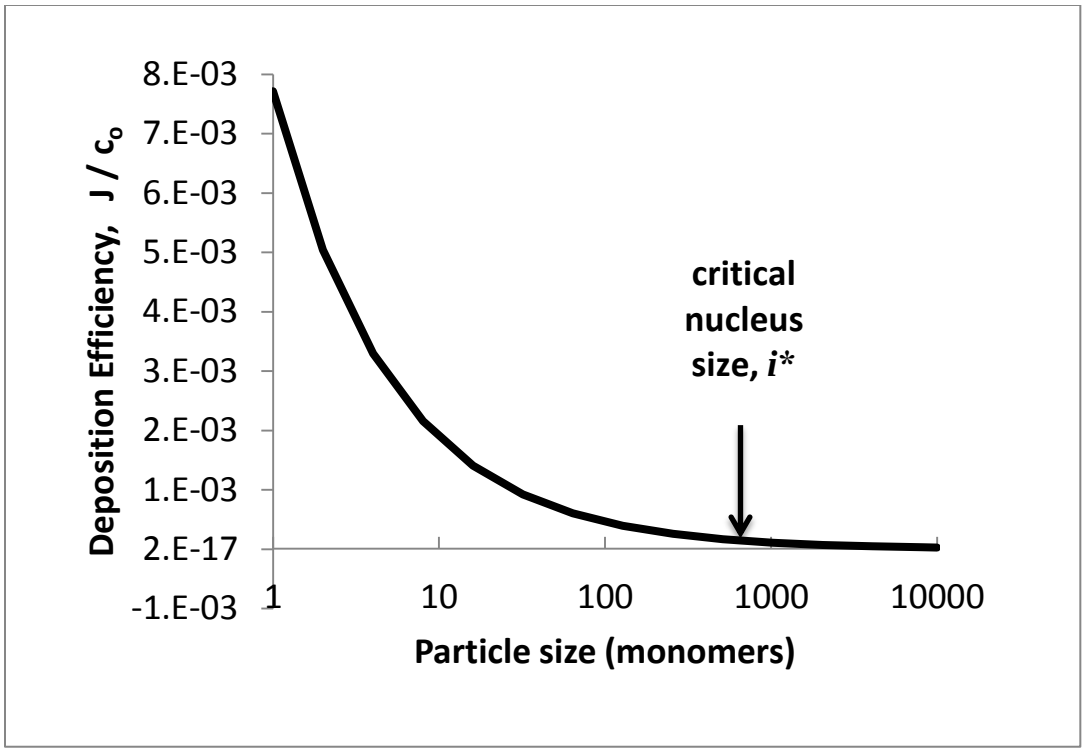

Figure 3.16
The deposition efficiency, defined as the fraction of particles incident on the static boundary layer that reach the liquid layer, depends on particle size. The data was calculated using Eq. 5 with U=1 ms^{-1}, T= 373 K, and P=1.36x10^{5} Pa.

Because the flux of material to the liquid layer is dominated by very small particles (with $Kn \gg 1$ where the Knudsen number Kn is the ratio of the mean free path of the gas molecules to the radius of the particle), we use the Epstein equation to compute the diffusion coefficient,[19]

$$D_i = \frac{3}{8\rho r_m^2 \delta}\sqrt{\frac{m_i kT}{2\pi}} \qquad (7)$$

where m_i is the particle mass, T is the temperature, $\delta = 0.91$ is the accommodation coefficient, and r_m is the particle mobility radius. For solid spherical particles, r_m is just the particle radius ($r_m = r_p$). However it is well established from studies of soot formation in hydrocarbon flames that the aggregation of gas-phase polycyclic aromatic hydrocarbons (PAH) leads to fractal-like, rather than compact particles.[20,21,22,23,24] Sorensen and coworkers[25] have shown that Equation 7 continues to provide a good description of diffusivity in the free molecular regime for fractal particles if the mobility radius is expressed in the form $r_m = r_1 i^x$, where r_1 is the radius of a monomer and x is the mass-mobility exponent. The exponent x has a fairly well established value for PAH aerosols[26,27,28] ($x = 0.46$), corresponding to particles with a fractal dimension $D_f \sim 1.8$. Equation 7 may therefore be rewritten as

$$D_i = A i^{1/2-2x} \tag{8}$$

where A is a constant.

In addition to their fractal-like morphology, aggregating PAH aerosols develop size distributions which exhibit dynamic scaling,[29] where the shape of the size distribution becomes time invariant and the average aggregate size increases in time t as $< i > \sim t^q$. The exponent q depends on the details of the aggregation process. To treat the effect aggregation on particle deposition efficiency, we approximate the particle size distribution as a δ-function centered at the average particle size and consider the

diffusive transport of that species across the static boundary layer. Since the amount of time particles have to aggregate before reaching the liquid layer is $t \approx dU^{-1}$, where d is the distance from the crucible to the substrate, Equations 5, 6, and 8 can be combined and written in terms of flow rate as:

$$J = c_o A' U^{\beta} \tag{5}$$

where A' is a constant and $\beta = (4xq - q)/3 + 1/2$.

Figure 3.17 shows a log-log plot of the experimentally measured deposition rate vs. jet velocity, where the slope is found to be $\beta = 0.89$. It can be seen that the deposition rate exhibits the expected power-law dependence on jet velocity, but that the slope is significantly larger than would be expected in the absence of aggregation (dashed line, $\beta = 1/2$). This suggests that some aggregation does take place in the gas phase. Based on a value of the mobility exponent $x = 0.46$, we find $q = 1.4$. This compares to a value of $q \approx 1$ resulting from solving the Smoluchowski equation for particle aggregation using the constant kernel model.[30]

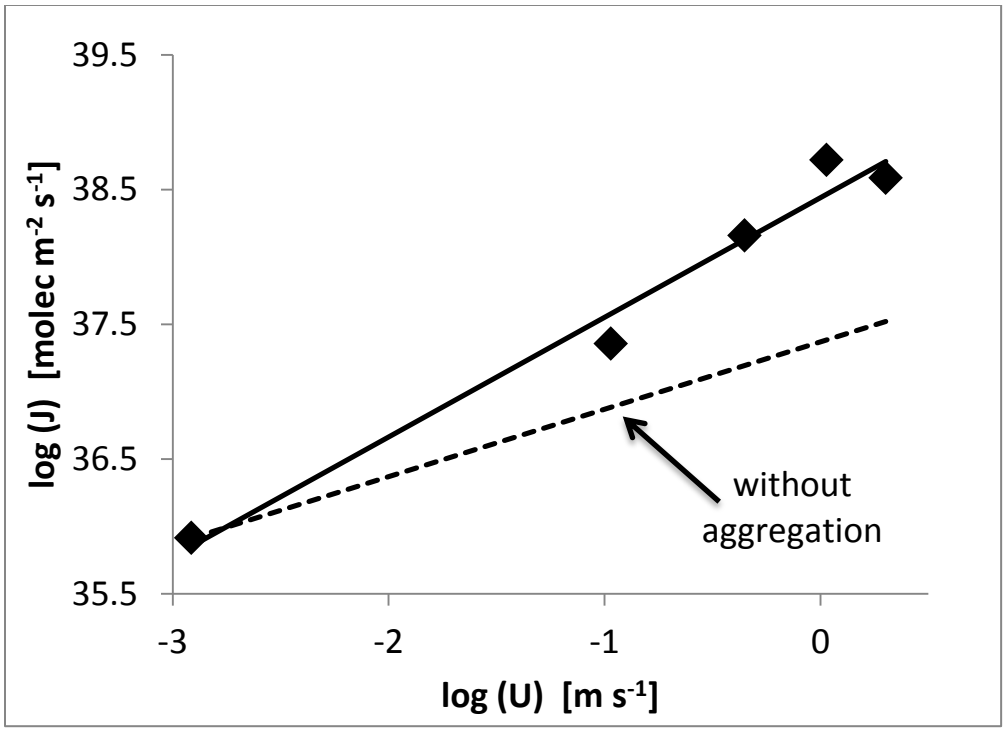

Figure 3.17
The deposition rate, J increases with flow rate as $J \sim U^{\beta}$, with $\beta=0.89$ (solid line), providing evidence for some aggregation of tetracene in the gas phase in transit to the substrate. In the absence of aggregation, the predicted exponent is $\beta=0.5$ (dashed line). Solid points are experimentally-measured deposition rates on 1 cm^2 bis(2-ethylhexyl)sebecate coated ITO glass substrates determined using UV-Vis spectroscopy with samples deposited using T=373 K, $P=1.36 \times 10^5$ Pa, z*=13 mm, needle radius a=1.91 mm.

3.5 Thermodynamic Analysis of Crystal Nucleation in Bis(2-ethylhexyl)sebecate

[Portions of this section are based on a manuscript in preparation by Shaw, D., Bufkin, K., Lund, C., Baranov, A., and Patrick D.L.]

As discussed below, the observed film growth kinetics are largely consistent with a diffusion-limited aggregation mechanism in which nuclei form in the liquid layer as a result of collisions between dissolved solute molecules and/or larger aggregates. For

heterogeneous crystallization of organic films at solid-vacuum and solid-gas interfaces the size of the critical nucleus i^* is typically small, in the range $i^* = 1 – 10$ molecules. In a liquid solvent however, solvation effects often lead to much larger values for i^*. This has a pronounced effect on growth kinetics by suppressing the nucleation rate, leading to fewer, but larger crystals. In the present system, where some aggregation of the tetracene aerosol appears to occur during transport in the vapor phase, knowledge of i^* is also important because any crystalline aggregates reaching the liquid layer that exceed this size may serve as new nuclei, offering a competing mechanism for crystal formation. In this section we analyze solubility measurements in terms of classical nucleation theory to provide an estimate for i^*.

From classical nucleation theory, the radius of a (spherical) critical nucleus is $a^* = 2s\Omega/\Delta\mu$, where s is the surface energy of the crystal-solvent interface, Ω is the molecular volume of the crystal, and $\Delta\mu$ is the difference in the chemical potential of a monomer in the crystal and one in solution. The surface energy can be estimated from $s \approx \Delta H_{diss}/s_a$, where ΔH_{diss} is the heat of dissolution per molecule and s_a is the surface area of one molecule. $\Delta\mu$ can be estimated from $\Delta\mu = kTln(C^*/C_{eq})$, where C^* is the concentration of tetracene in solution under the supersaturation conditions occurring during crystal nucleation, and C_{eq} is the equilibrium (saturation) concentration at the temperature of the substrate (20 °C).

We determined C^* from the induction time, that is, the length of time after deposition began before the first crystals appeared: $C^* = Ft_o/d_{solvent} + C_{eq}$, where F is the flux rate, t_o is the induction time, and $d_{solvent}$ is the solvent layer thickness. The equilibrium concentration appears in this expression because the induction time was measured with samples coated by a bis(2-ethylhexyl)sebecate layer that had been pre-saturated with tetracene, in order to reduce the time required to perform the experiment. From a set of three samples prepared under similar conditions we found $t_o = 2800 \pm 1100$ s for a flux rate $F = (1.7 \pm 0.5)$ x 10^{-9} mol m^{-2} s^{-1} and an average film thickness $d_{solvent} = 1.9 \pm 0.3$ μm. The latter was measured by interferometry as described in Chapter 2. C_{eq} was determined to be (7 ± 1) x 10^{-4} M (see below). Using these values we find $\Delta\mu = (6 \pm 1)$ x 10^{-21} J $molecule^{-1}$.

ΔH_{diss} was calculated from a series of temperature-dependent solubility measurements using the van't Hoff equation $ln\ x_{eq} = \Delta S/k - \Delta H_{diss}/kT$, where x_{eq} is the concentration at saturation measured as mole fraction of tetracene in bis(2-ethylhexyl)sebacate, and ΔS is the entropy of dissolution. These data are shown in Fig. 3.18. From the slope of the plot, $\Delta H_{diss} = (2.2 \pm 0.9)$ x 10^{-20} J $molecule^{-1}$. Using the approximation $s \approx \Delta H_{diss}/s_a$, we estimate surface energy to be $s \approx 46$ mJ m^{-2}.

Finally, based on these measurements we arrive at an estimate for the critical nucleus size $a^* \approx 4.3$ nm, or ~1000 molecules.

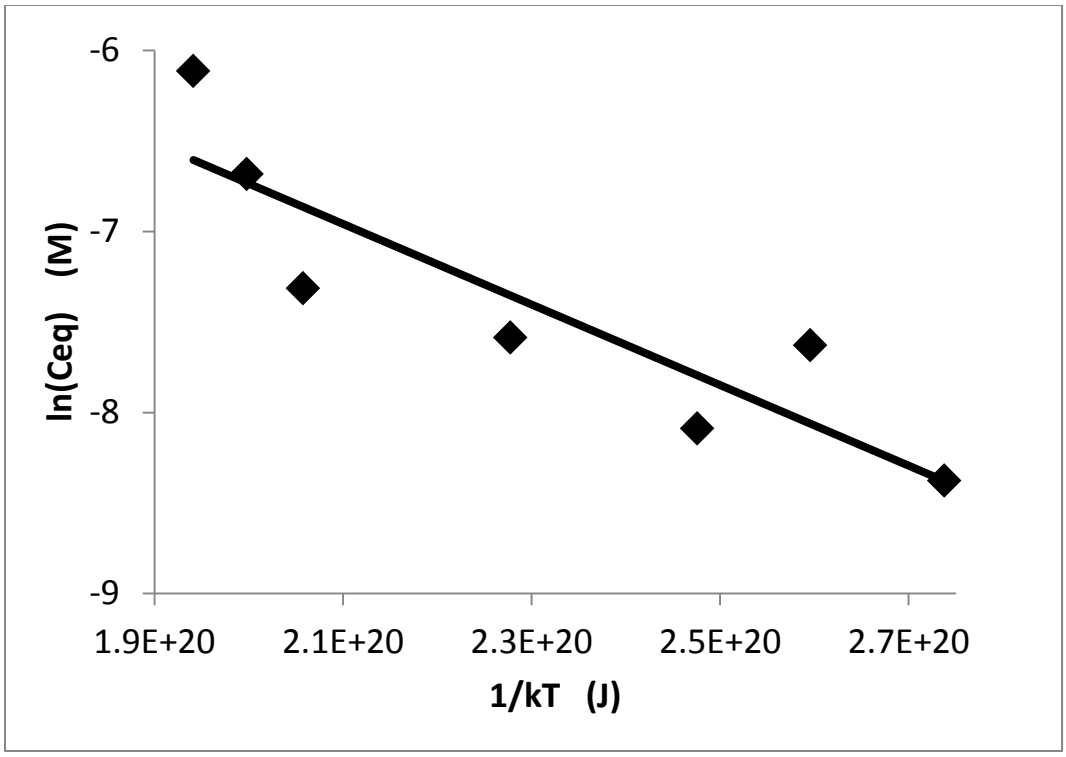

Figure 3.18
van't Hoff plot of the saturation concentration of tetracene in bis(2-ethylhexyl)sebecate vs. 1/kT. The slope equals the heat of dissolution. Concentration was measured by UV-Vis absorbance on a series of solutions equilibrated at range of temperatures between -8.5 °C and 100 °C.

In concluding this section, we note that the calculations assume the concentration of tetracene is uniform throughout the thickness of the solvent layer. However since the impinging tetracene arrives on the outer surface of the liquid, a certain concentration gradient is expected, with the highest concentration occurring at the vapor – liquid interface. To judge the significance of this effect, we compare the characteristic mixing time, τ, equal to the time required for a tetracene molecule to diffuse the thickness of the solvent layer, to the induction time, $t_o \sim 10^3$ s. The mixing time can be found by rearranging Einstein"s diffusion equation in 3-dimensions: $\tau =$

$\frac{d_{solvent}{}^2}{6D} \sim 10^{-2}$ s, where the diffusion coefficient is found from the Stokes-Einstein relation $D = kT/n\pi\eta r_1$, $\eta = 23 \times 10^{-3}$ N m^{-2} sec is the solvent viscosity, n is the molecular shape factor ($n \approx 4$ for an elongated molecule like tetracene[31]), and r_1 is the radius of a tetracene molecule. This gives $D = 3.5 \times 10^{-11}$ m^2 s^{-1}. Since $\tau \ll t_o$ the liquid layer can be taken as essentially uniformly mixed and we neglect the (consequently small) concentration gradient. If the system is fully mixed, it follows that deposition of new material can be thought of as occurring throughout the thickness of the liquid layer, as if new monomers were just as likely to materialize inside the fluid as at its surface. Hence the effective deposition rate depends on the thickness of the solvent layer, as originally pointed out by Sokolowski.

3.6 Preliminary Analysis of Crystal Growth Data

This section presents some preliminary analysis of crystal growth characteristics and behavior. Crystal growth data were collected with in situ cross polarizing optical microscopy. The images taken were analyzed using photoshop CS4 extended edition to calculate X and Y coordinates found at the onset of nucleation, crystal density, and the area of each crystal. Figure 3.19 shows a plot of crystal density vs. deposition time, i.e., time since deposition has started in minutes, as well as three important stages of time during deposition. The first is the saturation stage, in this stage no nucleation occurs, material is deposited onto the liquid layer and dissolved therein. Soon this liquid layer, in this case bis(2-ethylhexyl)sebecate, becomes supersaturated and reaches a critical point where crystals begin to nucleate; the nucleation stage.

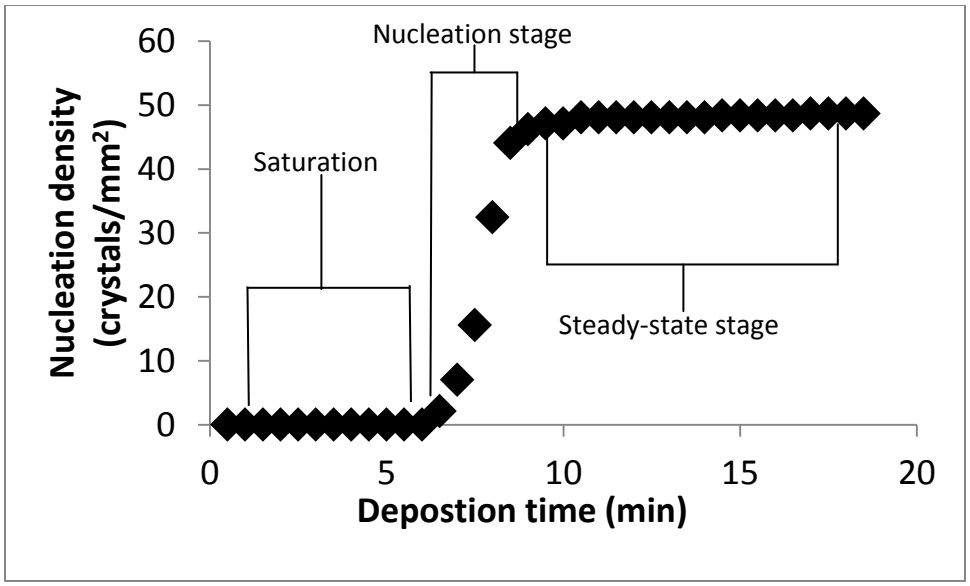

Figure 3.19
Plot of nucleation density in number of tetracene crystals per square millimeter in a thin film of bis(2-ethylhexyl)sebecate showing three stages during the growth of a film saturation, transient regime, and steady-state regime.

As can be seen from figures 3.19 and 3.20 during the nucleation stage crystal nucleate and grow quickly, this is because the supersaturated liquid surrounding the crystals rapidly adds material to existing crystals. Figure 3.20 shows the derivative of crystal density plotted against coverage, θ, (the fractional measurement of area covered by crystals /total area) highlighting the rapid nucleation of crystals to a coverage of 0.006. When the solution is no longer supersaturated the steady-state stage begins as shown in figure 3.19.

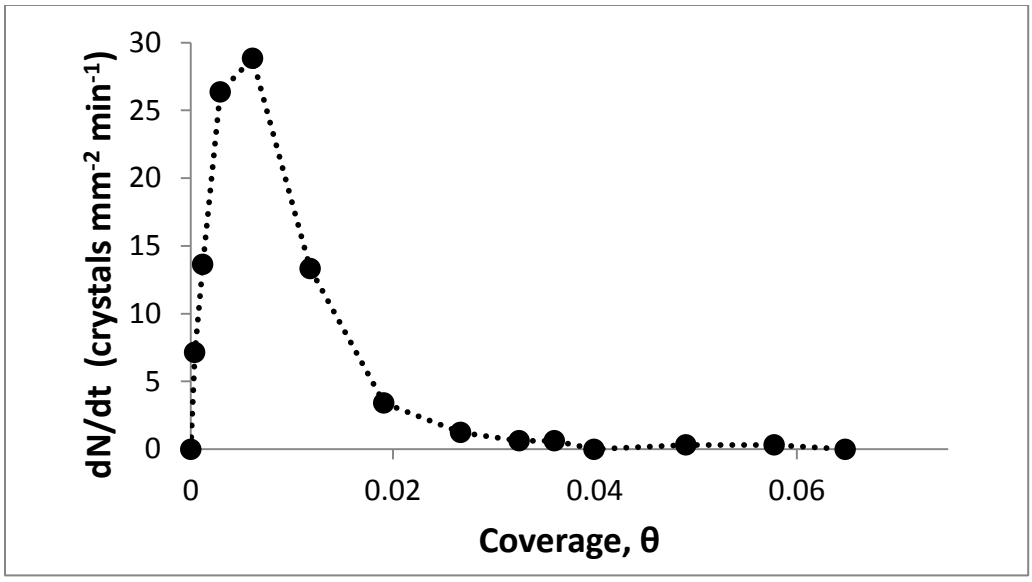

Figure 3.20
Crystal nucleation rate vs. coverage θ, defined as fractional surface area covered by crystals. After a critical concentration nucleation begins rapidly and after coverage θ=0.006 is reached nucleation rate declines to zero.

In this stage crystals are rarely nucleating, instead material is adding to already established crystals. It has been observed that in the nucleation stage the growth rate of crystals is higher than in the steady-state regime which follows it. This can be seen in figure 3.21 where a plot of coverage vs. deposition time is shown and there are two apparent growth rates that can be drawn from the data. Using the average height of a crystal calculated from AFM data presented in figure 3.7 the growth rates were calculated.

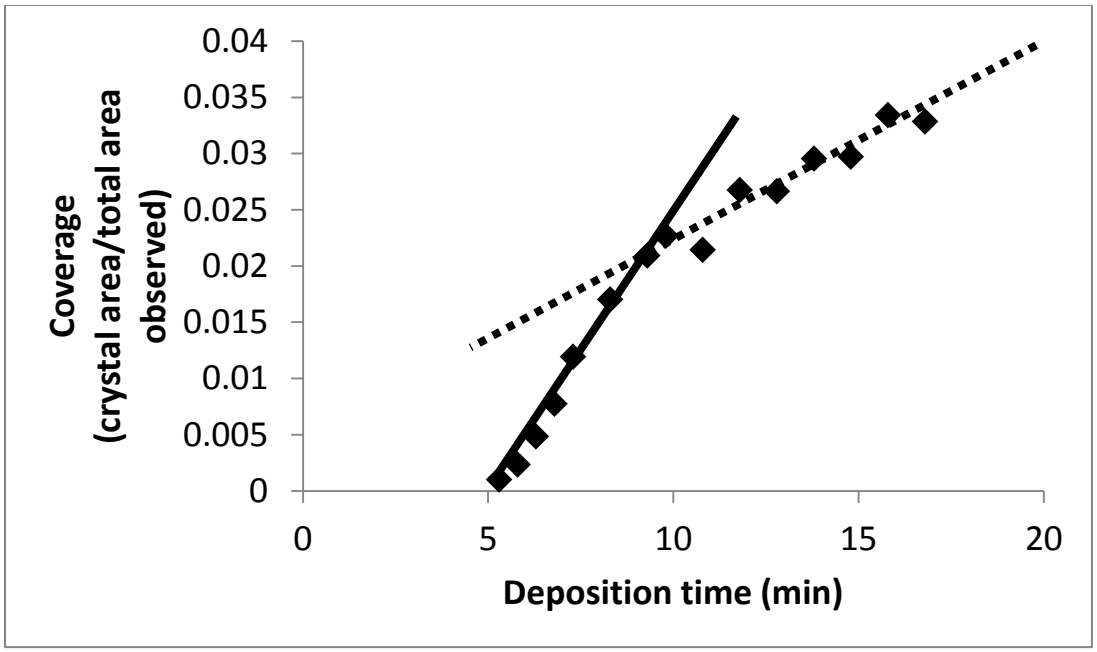

Figure 3.21
Coverage as crystal area/total area observed vs. deposition time in minutes. Film was grown in bis(2-ethylhexyl)sebecate showing the two different growth rates with one constant deposition rate. Lines in figure are not mathematically derived and are only present to emphasize the appearance of two rates.

Note, the AFM data presented was obtained from the same sample as figure 3.20 but the data from figure 3.19 is not from the same set as 3.20. The initial growth rate was found to be 3.64×10^{-8} mol/(sec m^2) and the secondary rate was found to be 1.26×10^{-8} mol/(sec m^2). The secondary growth rate is on the order of a reasonable flux rate but further work must be done to confirm. An interesting phenomenon is shown in figure 3.22, where both coverage and crystal density scale as approximately $\theta \sim N \sim t^{13}$ in the initial nucleation stage and then nucleation ceases and coverage scales linearly with time. Strictly 2D growth is predicted when coverage scales as $\theta \sim t^{1.0}$ this agrees with the AFM data shown earlier showing no dependence of crystal thickness on crystal area as well as fairly thin crystal growth at ~75nm.

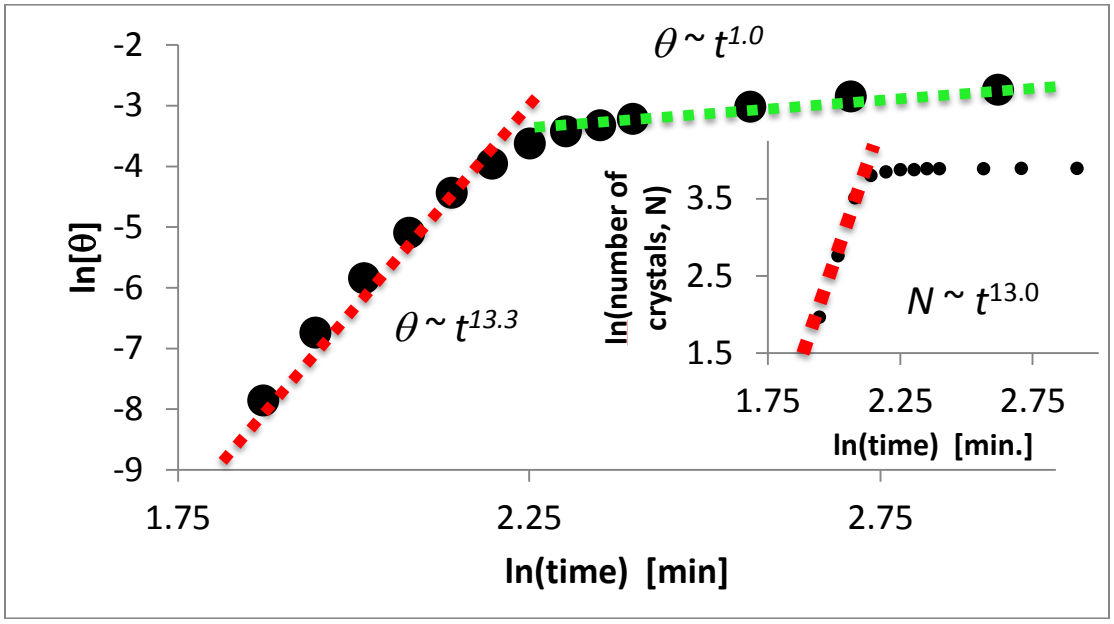

Figure 3.22
Plot of ln(coverage) vs. ln(time) showing two different dependences of coverage on time for two different stages $\theta \sim t^{13}$ and $\theta \sim t^{1}$ corresponding to the nucleation and steady-state stages. Shown in the inset is ln(number of crystals) vs. ln(time) note the initial dependence of $\theta \sim t^{13}$ during the nucleation stage.

X Y coordinates were used by a computer program to calculate the Voronoi tessellation shown in figure 3.23. Cells represent the area closest to a specific crystal associated with that cell instead of the neighboring crystals. The colors in figure 3.23 have no meaning other than to differentiate the cells from one another. The circles represent the relative size and positions of the crystals associated with each cell. Filled in circles represent crystals that are withheld from the analysis because the cell surrounding that crystal has an incompletely defined cell size because it intersects the outer boundary of analysis. The data obtained from the Voronoi cell tessellation can be analyzed in several different ways the first of which is a cell size distribution shown in figure 3.24.

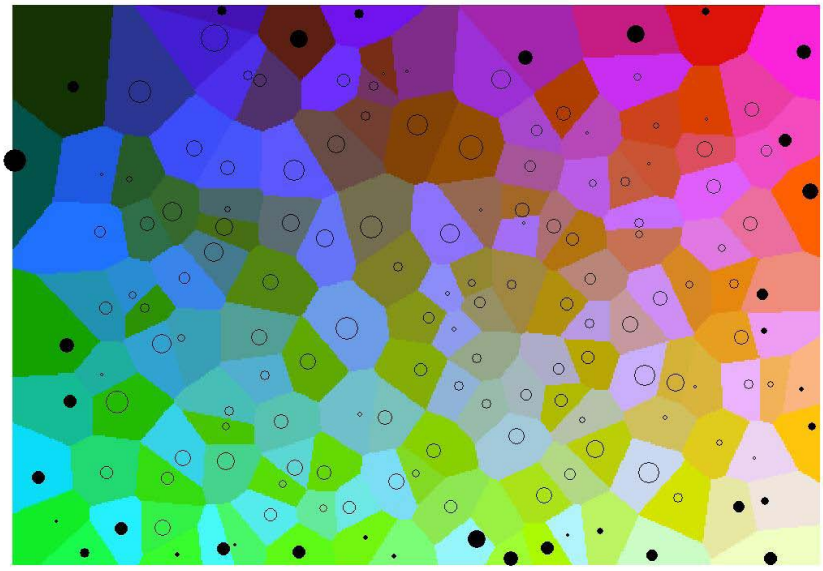

Figure 3.23
Voronoi tessellation circles show relative size (not to scale) and position of crystals. Cells with filled in circles intersected boundary and are excluded from analysis.

Figure 3.24 shows the cell size/average cell size plotted against a normalized probability as well as the semiempirical function $F\ y\ \approx \frac{\beta^{\beta}}{\Gamma\ \beta} y^{\beta-1} \exp\ -\beta y$ [32]plotted for two values of β (9.9 and 3.61). The solid line in figure 3.24 represents a β value of 9.9 which is the best fit for the experimental data and the dashed line represents a β value of 3.61 corresponding to a completely random cell size distribution.[33] Judging by the sufficient difference in β values and the difference in peak shapes from a broad short peak for the random distribution (β=3.61) to a much sharper and taller peak for the best fit experimental distribution (β=9.9), it is evident that the distribution of cells is not completely random.

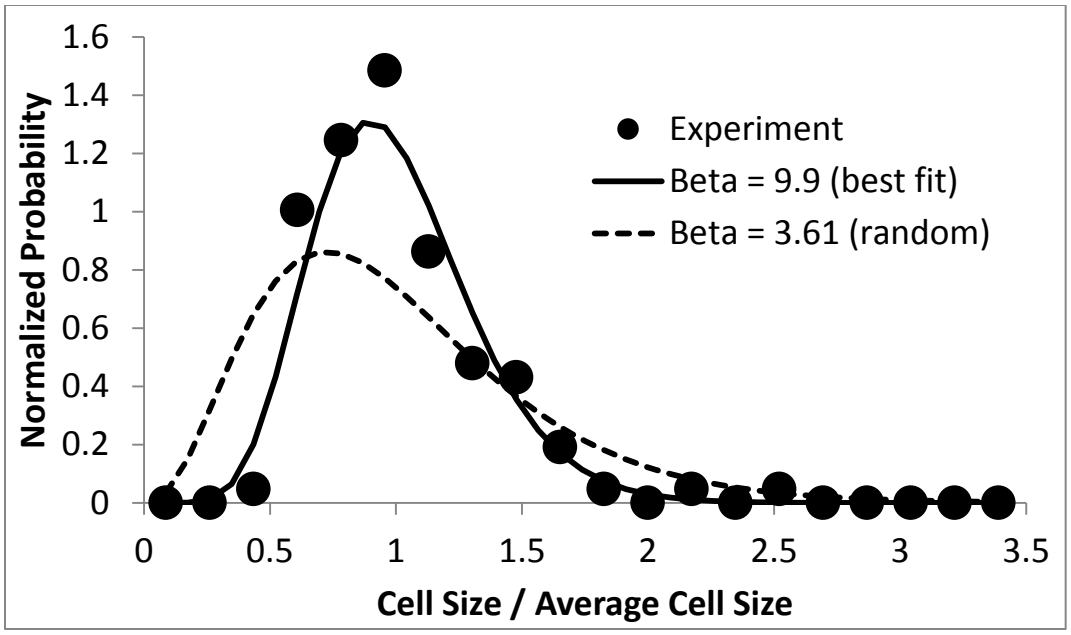

Figure 3.24
Voronoi cell size distribution, solid line is best fit to the data using the semiemperical function shown in text corresponding to a β value of 9.9. Dashed line is the distribution resulting from the tessellation of a collection of randomly positioned points, corresponding to a β value of 3.61

Other evidence to support the fact that the distribution of crystals is not completely random is shown is figure 3.25 as a radial distribution function of probability that a crystal will have a neighbor some distance away in μm. As can be seen in figure 3.25 crystals tend to not nucleate closer than 100 μm. This is consistent with the idea that crystals are using material from the surrounding liquid to nucleate and grow. If the solution around a crystal becomes locally depleted of organic semiconductor, lower than the critical concentration needed to nucleate new crystals, one should see a dependence on separation of nucleation sites similar to that shown in figure 3.25. The rate of crystal growth was found to depend on the size of the Voronoi cell, a plot of cell size vs. crystal growth rate is shown in figure 3.26.

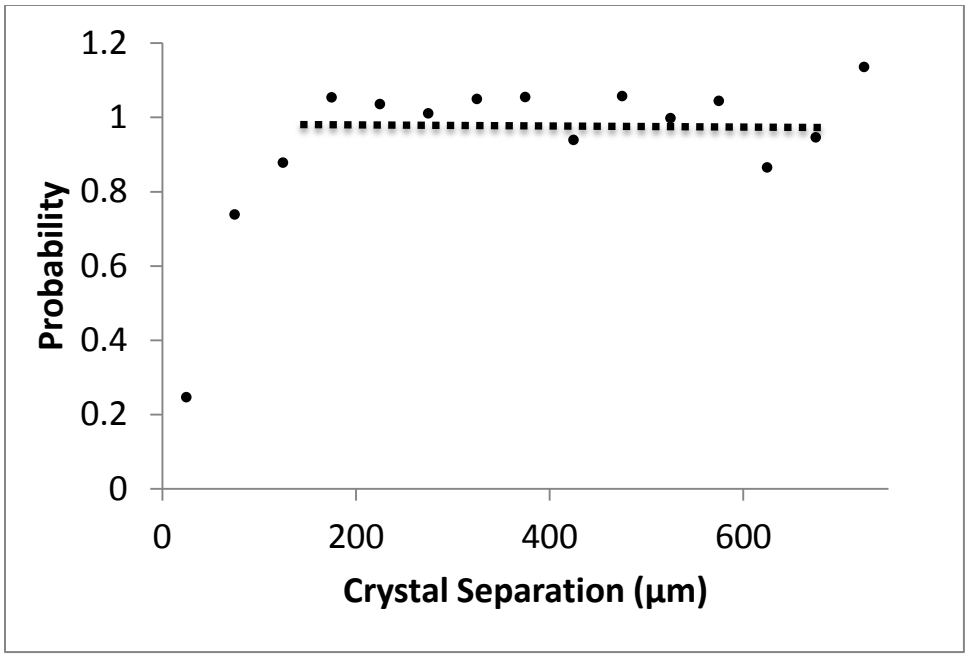

Figure 3.25
Radial distribution of crystal separation, probability that a crystal will have neighbor a given distance away, calculated with same program used to calculate Voronoi tessellation

The dependence of the crystal growth rate on Voronoi cell area is an important finding because it is evidence that the Voronoi cell area can be considered a capture zone. Capture zone being defined as an area in which flux landing in this area have a much higher probability of being incorporated into the crystal associated with that capture zone than any of its surrounding neighbors. Thus if a crystal had a very large capture zone and the incoming flux was uniformly depositing it would incorporate material from a very large area leading to a very large growth rate. All data used in figure 3.26 was taken during the steady state stage when the total change in coverage is approximately equal to the rate of deposition and growth is strictly 2D as shown by

figure 3.21 and 22. The growth rate of crystals is dependent on the size of its capture zone and therefore crystal sizes should follow a similar size distribution function.

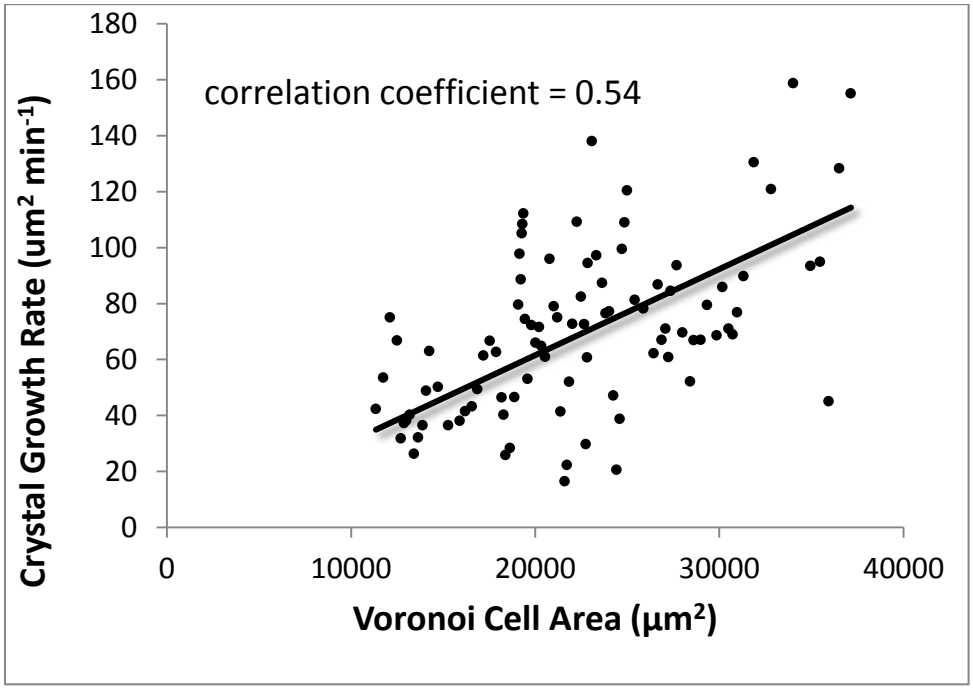

Figure 3.26
Relationship between crystal growth rate and Voronoi cell area, solid circles are a 3-point moving average after nucleation of new crystals had effectively ceased.

A histogram of crystal area at various times is shown in figure 3.27. Red and green dots represent data points collected at 10.5 and 18.5 minutes after deposition was started. Red and green dashed lines represent the best fit line to their respective red and green data points using the function $N(y) = A\frac{\beta^{\beta}}{\Gamma(\beta)}(y/a)^{\beta-1}exp\,(-\beta y/a)$ which as you can see is very similar to the function used for the Voronoi cell size distribution, this is consistent with the idea that the size distribution of crystals should have a similar distribution as the capture zone sizes. It can also be seen that during

the nucleation stage the size distribution does not fit the same function but does fit exponential decay quite well; this is shown in figure 3.27 with the blue dots

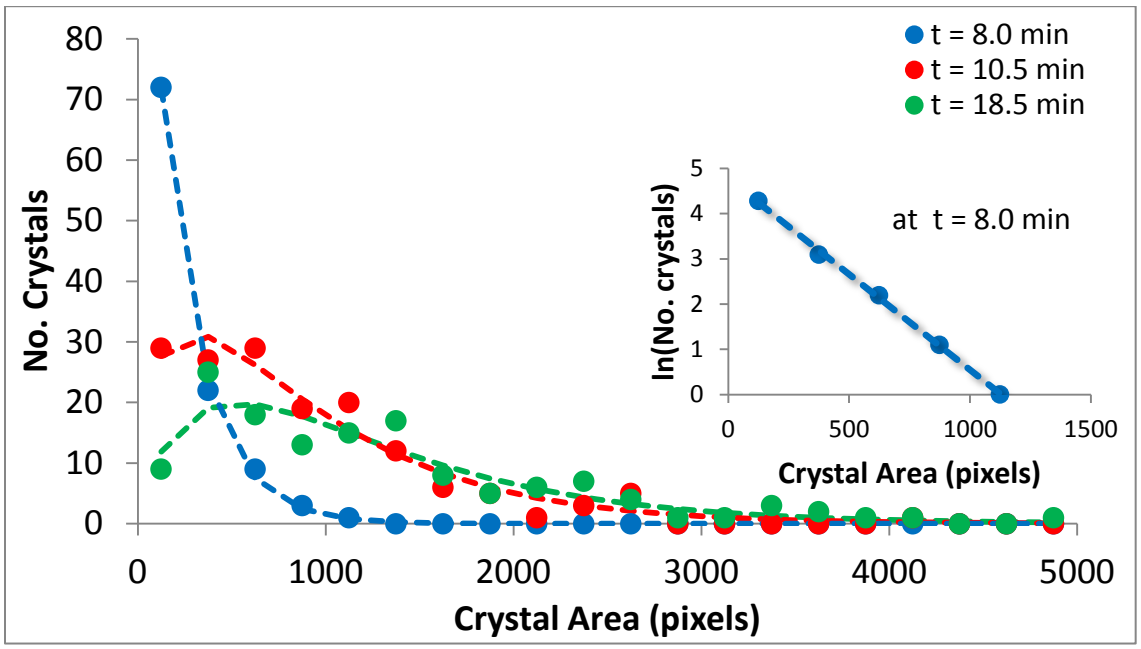

Figure 3. 27
Crystal size distributions at three different times. Points are experimental values. Blue line is a simple exponential. Red and green lines are best-fits to a semiempirical function similar to the one utilized in figure 3.26. inset shows that the initial size distribution is an almost perfect exponential. Inset data are for t = 8.0 min.

representing data points collected at 8.0 minutes after deposition was started during the nucleation stage, the inset is a plot of ln(number of crystals) vs. the crystal area for data collected at 8.0 minutes after deposition. This is consistent with supersaturation and an initial explosion of nucleation when crystals are at a size where they can be counted but their size cannot yet accurately be judged via the detection method used.

3.7 Conclusions and Future Work

In summary it has been found that for the method described sublimed tetracene vapor aggregates before reaching the static boundary layer, but the sizes of aggregates that deposit onto the liquid layer are below the critical nucleation size. The aggregates that arrive at the liquid layer are dissolved, eventually forming a supersaturated solution during the saturation stage. Once this supersaturated solution reaches a critical concentration nucleation and crystal growth begin rapidly during the nucleation stage. After the liquid layer‟s concentration of tetracene has been reduced to its equilibrium concentration the steady-state stage starts, where nucleation ceases and the rate of growth of crystals is approximately equal to the rate of deposition. Growth continues in this manner until crystals begin to grow into each other and coalesce.

This thesis delineates the refinement of a method and theory to describe the processes utilized for the deposition of quality organic semiconductor thin films. Growth of these thin films was improved with the use of a liquid layer. The basic characterization of the thin films produced by this method has been established and agrees with the theory presented in this thesis. A kinetic basis for the stages of growth was found combining elements of classical crystallization and diffusion limited aggregation theory.

Future work will include modification of the method, e.g., employment of different liquid layers, i.e., novel oriented liquid crystals, different substrate temperatures and alteration to the chamber to reduce the amount of 5,12-napthacenequinone produced during sublimation and deposition. Quality films will be rinsed with cold hexanes to

remove the liquid layer and electrodes will be patterned on to the film to test the electronic properties of the thin films. Several different organic semiconductors will be used to make thin films with the same method such as pentacene, rubrene, and C60.

---

[1] M. Voigt, S. Dorsfeld, A. Volz, M. Sokolowski, phys. Rev. let. **91**, 026103 (2003)

[2] Kevin Bufkin, MS thesis, Western Washington University, Bellingham, WA, 2010

[3] A. Rubel, AIAA J. **21**, 351 (1983).

[4] H. W. Smith, R. A. Schmitz, and R. G. Ladd, Comb. Sci. Technol. **4**, 131 (1971).

[5] "Laboratory Studies of Volcanic Jets", Kieffer, A. W.; Sturtevant, B., J. Geophys. Res. 1984, 89, 8253.

[6] Reynolds, A. J. : Observations of a Liquid-Into-Liquid Jet. pt. 4, Dec. 1962, pp. 552-556.

[7] Andrade, E. N. da C. ; and Tsien, L. C. : The Velocity-Distribution in a Liquid-Into-Liquid Jet. Proc. Phys. SOC., vol. 49, pt. 4, July 1937, pp. 381-391.

[8] "Observations of a liquid-into-liquid jet", Reynolds, A. J.; J. Fluid Mech. 1962, 14, 552.

[9] H. Schlichting, „„Laminare strahlenausbreitung,"" Z. Angew. Math. Mech. **13**, 260, 1933.

[10] Kwon, S. J. & Seo, I.W. 2005 Reynolds number effects on the behaviour of a non-buoyant round jet. Exp. Fluids 38, 801–812.

[11] H. Schlichting, *Boundary layer theory* (McGraw-Hill Book Company, Inc., New York, 1960).

[12] D. F. Rogers, Laminar Flow Analysis, Cambridge University Press, Cambridge, UK (1992)

[13] J. Mater. Res. 1997, 12, 1112

[14] Shtein, M.; Gossenberger, H. F.; Benziger, J. B.; Forrest, S. R., "Material transport regimes and mechanisms for growth of molecular organic thin films using low-pressure organic vapor phase deposition", J. Appl. Phys. 2001, 89, 1470.

[15] Chin, D-T.; Tsang, C-H., "Mass transfer to an impinging jet electrode", J. Electrochem. Soc.: Electrochem. Sci. Technol. 1978, 125, 1461.

[16] D. W. Cooper, M. H. Peters, R. J. Miller, *Aerosol Sci & Technol*. **11**, 133 (1989).

[17] Michael H. Peters, Douglas W. Cooper and Robert J. Miller, "The Effects of Electrostatic and Intertial Forces on the Diffusive Deposition of Small Particles onto Large Disks: Viscous Axisymmetric", J. Aerosol Sci., Vol. 20, No. 1, pp. 123 136, 1989

[18] Shtein, M.; Gossenberger, H. F.; Benziger, J. B.; Forrest, S. R., "Material transport regimes and mechanisms for growth of molecular organic thin films using low-pressure organic vapor phase deposition", J. Appl. Phys. 2001, 89, 1470.

[19] "Diffusion of fractal aggregates in the free molecular regime", Cai, J.; Sorensen, V. M., Phys. Rev. E 1994, 50, 3397.

[20] Soot aggregates, superaggregates and gel-like networks in laminar diffusion flames, Wongyo Kim, Christopher M. Sorensen, Danny Fry, Amitabha Chakrabarti, Aerosol Science 37 (2006) 386–401

[21] K.A. Jensen, J.M. Suo-Antilla, L.G. Blevins, Measurement of soot morphology, chemistry, and optical properties in the visible and near-infrared spectrum in the flame zone and overfire region of large JP-8 pool fires, Combust. Sci. Technol. 179 (2007) 2453–2487.

[22] U.O. Köylü, G.M. Faeth, T.L. Farias, M.G. Carvalho, Fractal and projected structure properties of soot aggregates, Combust. Flame 100 (1995) 621– 633.

[23] Rajan K. Chakrabarty, Hans Moosmu¨ller, W. Patrick Arnott, Mark A. Garro, Guoxun Tian, Jay G. Slowik,

Eben S. Cross, Jeong-Ho Han, Paul Davidovits, Timothy B. Onasch, and Douglas R. Worsnop, "Low Fractal Dimension Cluster-Dilute Soot Aggregates from a Premixed Flame", Phys. Rev. Lett. 102, 235504 (2009) and references therein.

[24] Li, X.; Logan, B. E., "Collision Frequencies between Fractal Aggregates and Small Particles in a Turbulently Sheared Fluid", Environ. Sci. Technol. 1997, 31, 1237.

[25] "Diffusion of fractal aggregates in the free molecular regime", Cai, J.; Sorensen, V. M., Phys. Rev. E 1994, 50, 3397.

[26] Cai, J. and Sorensen, C. M. (1994) Diffusion of fractal aggregates in the free molecular regime. Phys. Rev. E 50, 3397

[27] GM Wang, CM Sorensen, Diffusive Mobility of Fractal Aggregates over the Entire Knudsen Number Range, Physical Review E. 60 (1999) 3036-3044.

[28] Sorensen, C. M., "The mobility of fractal aggregates: A Review", Aerosol Sci. Technol. 2011, 45, 755.

[29] Weitz, D. A.; Lin, M. Y., "Dynamic scaling of cluster-mass distributions in kinetic colloid aggregation", Phys. Rev. let. 1986, 57, 2037.

[30] Cohen, R. J.; Benedek, G. B., J. Phys. Chem. 1982, 86, 3696.

[31] *The Mechanisms of Fast Reactions in Solution*, Caldin, E. F., 2001, (IOS Press, Amsterdam, The Netherlands)

[32] WEATRED L., KERMODEJ,. P., WEICHERJ T., **1986,** *Phil. Mag.* B, 53, LlO1

[33] Mulheran, P. A.; Blackman, J. A., Phil. Mag. Lett. 1995, 72, 1.